Evaluation of Caprock Integrity of the Upper Ordovician Units within the CarbonSAFE Prefeasibility Study Region
Subtask 4.3 – Geological Characterization
Topical Report

March 1, 2017 through May 30, 2019

Cristian R. Medina[1], John A. Rupp[2], Richard Lahann[1], and Jayson Eldridge[1]

[1]Indiana Geological and Water Survey, Indiana University, 420 N. Walnut Street, Bloomington, IN 47404

[2]O'Neill School of Public and Environmental Affairs Indiana University, 1315 E. Tenth Street, Bloomington, IN 47405

Report Issued:
May 23, 2019

Report Number: DOE-FE0029445-11
U.S. DOE Cooperative Agreement Number: DE-FE0029445
CARBONSAFE ILLINOIS EAST SUB-BASIN

Principal Investigator: Dr. Hannes Leetaru
Business Contact: Illinois State Geological Survey
615 E. Peabody Drive
Champaign, IL 61820-7406

Executive Summary

In this report, the Indiana Geological and Water Survey (IGWS) evaluates the seal capacity of the Maquoketa Shale Group, a thick and heterogeneous sequence of carbonates, silts, and clay-rich rock units of Upper Ordovician age. This unit has been identified as a regional caprock that can effectively isolate the CO_2 stored in underlying reservoirs for secure sequestration. To accomplish this objective, the Maquoketa Group was assessed using two approaches: (1) development of a lithofacies/qualitative permeability model based on the combined wireline responses, and (2) analysis to characterize the pore size distribution and capillary entry pressures of the various lithologies in the unit using the mercury injection capillary pressure method.

Table of Contents

1. Introduction

In reservoirs used for CO_2 storage, following injection of supercritical CO_2, a portion of this fluid will migrate upward within the formation because of buoyancy forces. The mobile plume of CO_2 fluid ultimately accumulates against the caprock, which prevents further vertical movement (Bentham and Kirby, 2005). In the absence of significant structural traps, the injected CO_2 then will migrate laterally by combined dispersion and advection along the hydraulic gradient. However, flow velocities in deeply buried geologic units typically occur at rates measured in meters per hundreds or thousands of years.

The potential of the Maquoketa Group (Ordovician) to effectively function as a seal for permanent sequestration of CO_2 was evaluated using two methods: (1) a qualitative assessment of the bulk permeability based on the type of rock or 'lithofacies' present in the unit and (2) a quantitative assessment of the pore size distribution and entry pressures of CO_2 in samples of the defined lithofacies. The first effort of this evaluation resulted in the development of a wireline log-based model (aka lithofacies model) that subdivides the Maquoketa Group into five interpreted lithofacies: (1) limestone; (2) muddy limestone; (3) calcitic/dolomitic shale; (4) silty shale; and (5) shale. For practical reasons and visualization purposes, we have grouped lithofacies 1–2 and 3–5 to generate subdivisions of carbonate-rich and clastic-dominated facies, respectively. For calibrating and verifying this model, we used data collected from different sources: a statistically interpreted model (Elemental Log Analysis or ELAN model), core samples, drill cuttings, and portable X-ray fluorescence (pXRF) analyses. The lithofacies model suggests that the Maquoketa Shale Group is dominated by silty shale and calcitic/dolomitic shale with subordinate amounts of muddy limestone, limestone, and shale.

The mapped lithofacies suggest that the Maquoketa Group can be subdivided into three major units (upper clastic, middle carbonate, and lower clastic), and that clay content and overall thickness of the lower unit of the Maquoketa Group increases from west to east. The lower unit is the most important seal because it would be in direct contact with CO_2 injected into underlying reservoirs. This wireline log-based lithofacies model, when combined with petrophysical properties obtained from mercury injection capillary pressure (MICP) analysis, identifies areas having higher potential for effective confinement and quantifies the effectiveness of this seal for confining CO_2 injected into the underlying reservoirs.

2. Study Area—CarbonSAFE Illinois Basin

This report provides a regional assessment of the seal capacity of the Maquoketa Group located within the eastern Illinois Basin CarbonSAFE area and includes portions of the states of Illinois and Indiana (Figure 2.1). The subsurface geology of this region can be described as a thick sequence of relatively undeformed Paleozoic rocks lying unconformably on Precambrian basement. The stratigraphic sequence under evaluation within the Cambrian-Ordovician storage complex is shown in Figure 2.2. Several units shown in Figure 2.2 have previously been identified as potential targets for geologic sequestration (Medina et al., 2011; 2017; Greb et al., 2012; Medina and Rupp, 2012; Ellett et al., 2013). The top of the Maquoketa Shale Group is deeper than the recommended minimum depth of 2,500 ft in most of the study area (Appendix C: Figure C.1). At 2,500 or deeper, the CO_2 will be in its dense phase (liquid or supercritical).

Previous studies on the Upper Ordovician Maquoketa Group suggest that this sequence is a heterogeneous succession composed of fine-grained and thinly bedded lithologies, including both clastics (mudstones and siltstone) and carbonates (limestone/dolomite) (Gray, 1972; Kolata and Nelson, 1991). In this context, regional variation in lithological character has a direct impact on the petrophysical properties of the Maquoketa Group, such as the caprock integrity and seal efficiency. In this work, we developed a log-based lithofacies model that can help quantify the relative abundance of lithologies. In addition, petrophysical testing including mercury porosimetry and core analyses aid in the characterization of the Maquoketa Shale Group by looking at the capillary entry pressure and permeability of this sequence.

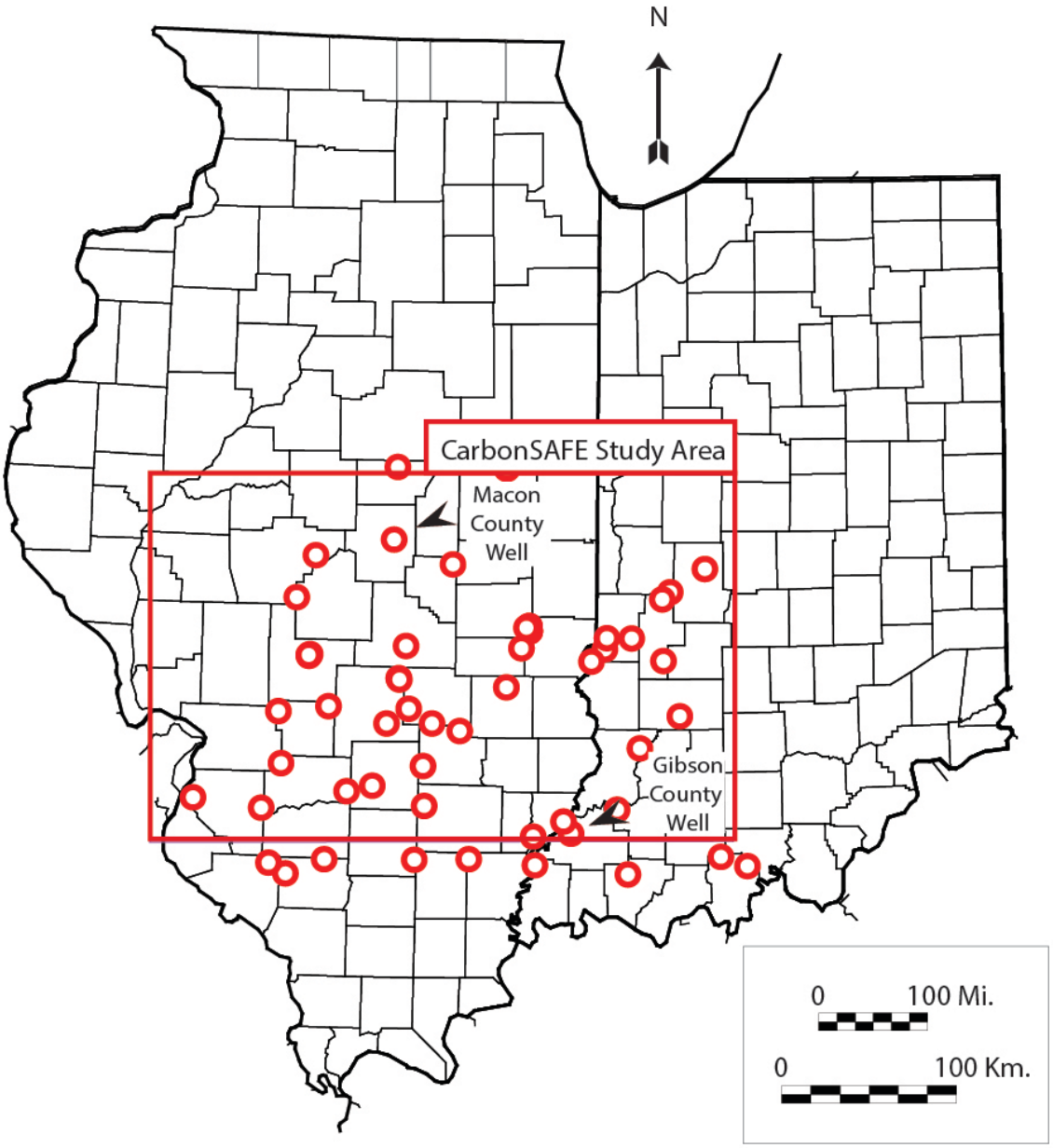

Figure 2.1. Map of the study area indicating wells with geophysical logs used to develop a lithofacies model (section 3). The red rectangle indicates the prefeasibility study area. Wells outside the study area were also used to aid in the lithofacies interpretation.

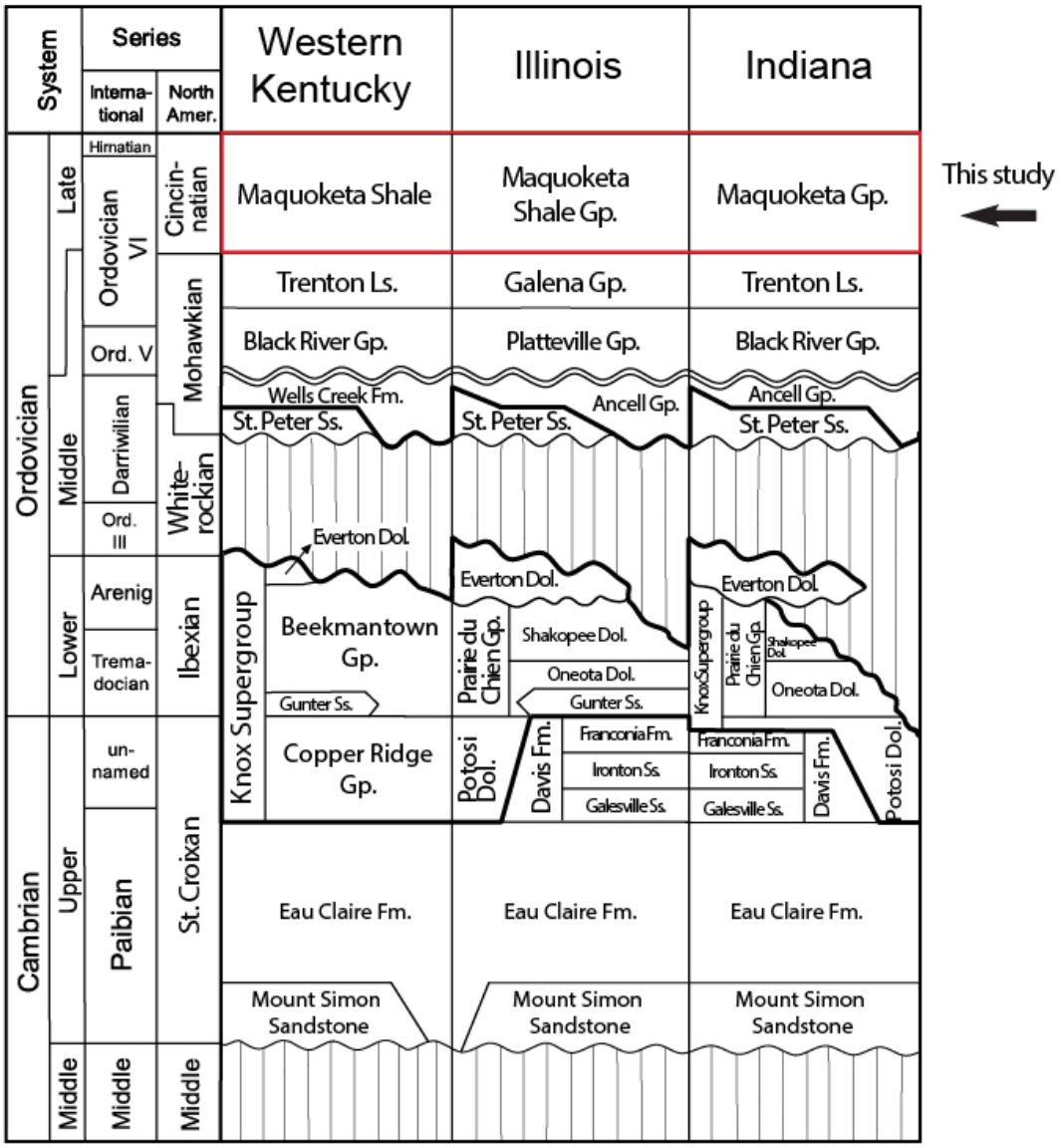

Figure 2.2. Stratigraphic chart indicating the stratigraphic context of the samples under study, which are part of a regional-scale caprock unit. Modified from Greb et al., 2012.

3. Methodology and Results

In this work, we integrated data from thin sections, X-ray diffraction (XRD), portable X-ray fluorescence (pXRF), mercury porosimetry (MICP), and geophysical logs. The model used data from geophysical logs to generate the interpreted lithofacies. We calibrated these results with interpreted mineralogy from pXRF data. For a complete list of wells and petrophysical analyses run on each sample, see Tables B.1 and B.2 (Appendix B), respectively.

3.1. Lithofacies Model from Wireline Logs

The objective of the wireline project was to create a regional-scale lithological model of part of the Illinois Basin, based on the wireline response of gamma-ray (GR), neutron (NPHI), and density (RHOB) logs. When combined, these logs can be used to interpret the major lithologic component of the vertical section under analysis (Asquith and Gibson, 1982). Two control well locations where the mineralogical composition was previously interpreted were used to calibrate the log-based interpretations. These wells are here referred to as (1) the Macon County, Illinois, well and (2) the Gibson County, Indiana, well. The log-based lithologic model describes the lithofacies abundance and is applied to multiple wells having the appropriate log suite to create a lithofacies model for the specific study area (Figure 2.1).

The well located in Macon County, Illinois is important because it has an Elemental Log Analysis (ELAN) log, which is a probabilistic mineralogical model based on the observed log response from multiple borehole geophysical tools based on known values of mineral responses to such tools. Analysis of the ELAN model at the Macon County well location indicates the presence of two intervals of high (> 50 %) calcite abundance, which are interpreted as 'clean' limestone (Figures 3.1–3.2). The only clean limestone interpretations in the Gibson County, Indiana, well (129758[1]) (based on high calcium content as shown by pXRF data from this control well) are associated with the transition into the overlying Upper Silurian limestone and the underlying Trenton Limestone. With this information, and applying a maximum threshold of gamma-ray values of 80 American Petroleum Institute (API) units for limestone, we determined the neutron-density field for limestone.

The ELAN analysis from the Macon County well indicates an interval of clay abundance near 40 %, with quartz as the second most abundant mineral (Figure 3.2A; depth 2,612–2,660 ft); this interval is interpreted as silty shale. The ELAN analysis also indicates multiple intervals with clay abundance near 50 % and either dolomite or calcite as the second most abundant mineral (Figure 3.2A; depth 2,735–2,812 ft). These intervals are interpreted as calcitic/dolomitic shale.

Additionally, we used pXRF data from a well in Gibson County, Indiana, located near the southeast corner of the focus area (Figure 2.1). The calcium (Ca) plot shows that the abundance of this element in the lower interval of the Maquoketa (~5,225–5,425 ft depth) is about 50 % of the value in the overlying Upper Silurian limestone and underlying carbonates from the Trenton intervals (Figure 3.2B). We interpreted this interval as muddy limestone.

The Ca/Mg ratio from a well in Gibson County indicates a calcite/dolomite ratio between 7:1 and > 20:1 in the same depth interval (depth ~5,225–5,425 ft; Figure 3.2B). Based on the calcite/dolomite ratio and

[1] The well number is from the Indiana Geological and Water Survey Petroleum Database Management System.

the overall abundance of Ca, the lower Maquoketa interval at this location is interpreted to contain muddy limestone.

The data in Figure 3.2B also shows that lower Ca/Mg ratios suggest that dolomitic-rich facies occur primarily in the upper Maquoketa interval. This pattern is consistent with the association of dolomite in the Macon County, Illinois, well (Figure 3.1) with clay-rich intervals.

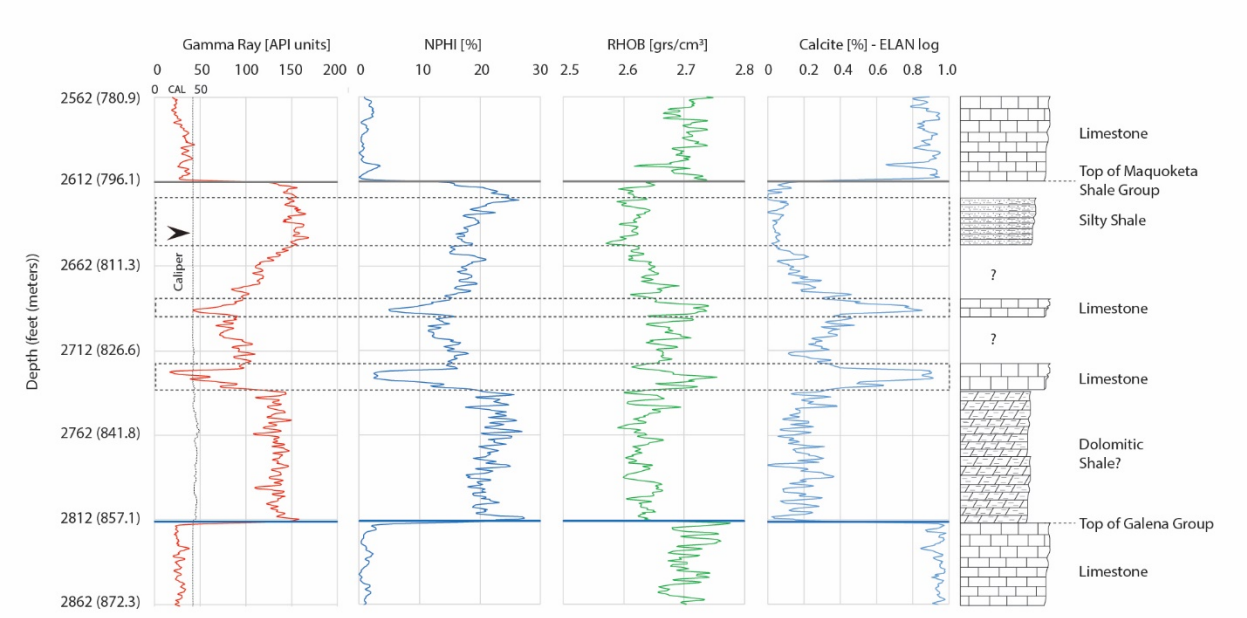

Figure 3.1. Wireline logs and electric (ELAN) log of calcite content in the Macon County, Illinois, well.

The Ca content of the Gibson County, Indiana, well (Figure 3.2B) shows that the lower portion of the Maquoketa Group (5,225–5,420 ft) has a Ca content 40–60 % of the Ca content of the over- and underlying limestones. The decreased Ca content and the increased gamma-ray and neutron porosity relative to the clean Lower Silurian limestone and the Trenton Limestone (Ordovician) suggest that the lower Maquoketa contains substantial amounts of muddy limestone (Figure 3.2B). Similar to that used to define neutron-density features of clean limestone, the neutron-density properties of the interval from 5,225 to 5,430 ft in the Gibson County well were used to define the neutron-density field for muddy limestone (Figure 3.3). The combined information of wireline logs (gamma-ray, neutron, and density), ELAN logs, and pXRF allows the determination of several lithofacies fields in a crossplot of the density and neutron data (Figures 3.3–3.4).

Careful examination of the neutron, density, and gamma-ray log data from the Macon County, Illinois, well (Figure 3.1) shows that the silty shale and calcitic/dolomitic shale show no significant distinction on the neutron and density logs. However, the calcitic/dolomitic shale interval has a slightly higher gamma-ray response. Therefore, a gamma value of 140 API units was chosen to distinguish them. In addition, calcitic/dolomitic shale was interpreted as having higher neutron responses than the muddy limestone line (Figure 3.1). In the upper section of the Macon County well, both clean shale and silty shale have gamma-ray logs above 140 API units, but depths having a neutron porosity response greater than 0.235 (-) were assigned as shale (Figure 3.3).

These three lithologies are shown for the Macon and Gibson County wells (Figure 3.2). The unusually high neutron porosities above the silty shale (Figure 3.2B) are most likely owing to a washout, and no lithologic assignment was chosen for these intervals.

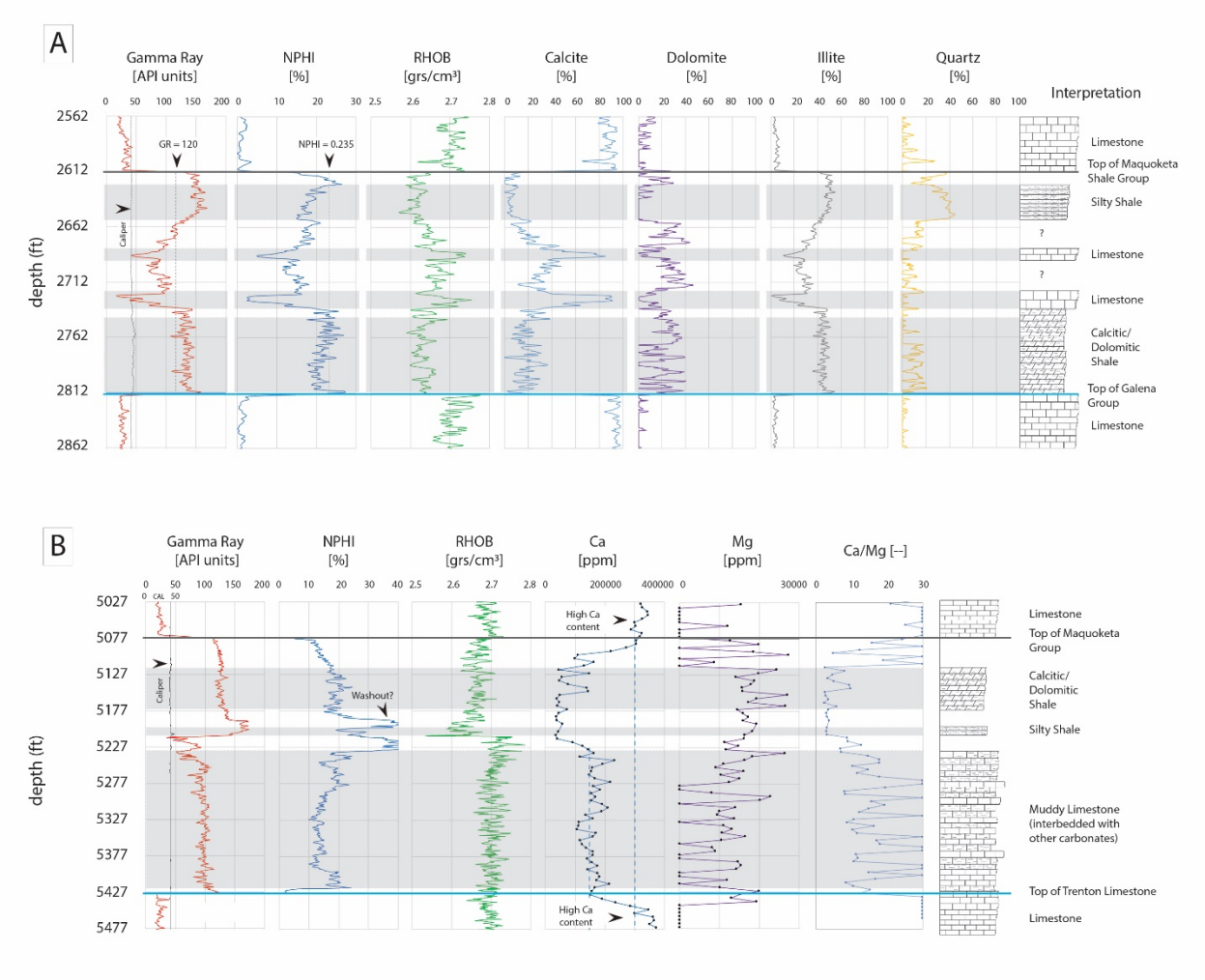

Figure 3.2. (A) Wireline logs and mineral interpretation (ELAN) in the Macon County, Illinois, well; (B) Wireline logs and pXRF data for calcium (Ca), magnesium (Mg), and their ratio in the Gibson County, Indiana, well. For the purpose of calculating the Ca/Mg ratio, when Mg is low and/or undetected, we assigned a value of 30.

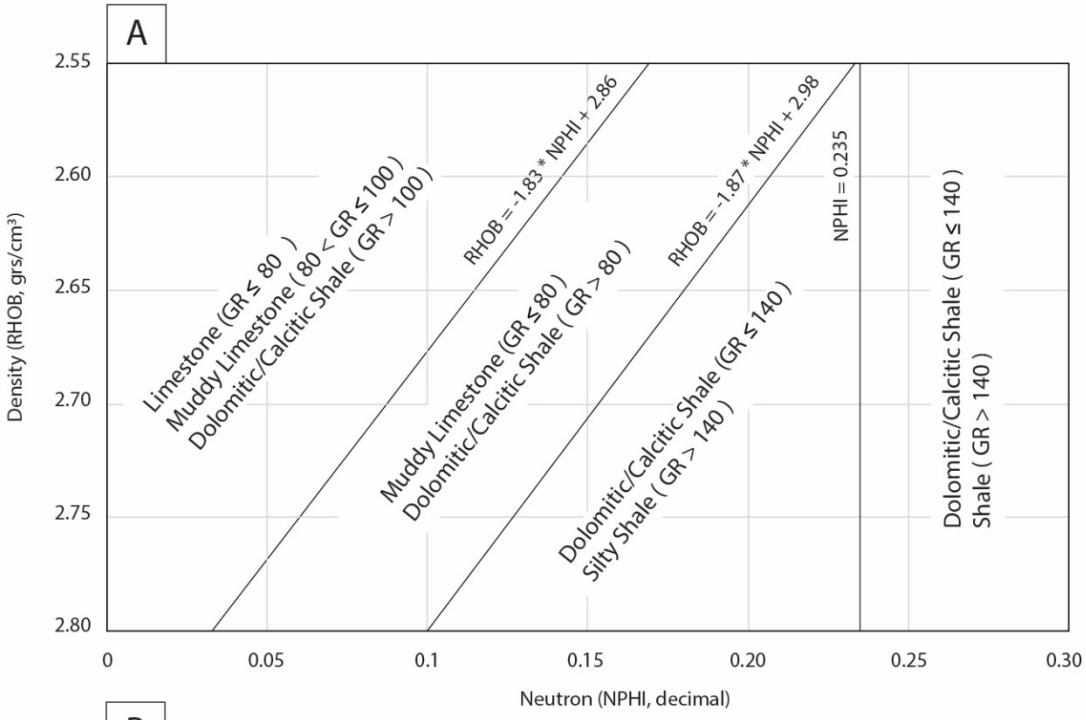

B

Lithofacies	Gamma Ray (GR)	Neutron Porosity (NPHI)	Density (RHOB)
Limestone	GR ≤ 80	n.a.	≤ density(dolomite)
Muddy Limestone	80 < GR ≤ 100	n.a.	≤ density(dolomite)
	GR ≤ 80	n.a.	density(dolomite) ≤ RHOB ≤ density(dol/cal shale)
Dolomitic/Calcitic Shale	GR > 100	n.a.	≤ density(dolomite)
	GR > 80	n.a.	density(dolomite) ≤ RHOB ≤ density(dol/cal shale)
	GR ≤ 140	NPHI ≤ 0.235	density(dol/cal shale) ≤ RHOB
	GR ≤ 140	NPHI > 0.235	density(dol/cal shale) ≤ RHOB
Silty Shale	GR > 140	NPHI ≤ 0.235	density(dol/cal shale) ≤ RHOB
Shale	GR > 140	NPHI > 0.235	density(dol/cal shale) ≤ RHOB

Figure 3.3. Cross plot chart with fields of interpreted lithofacies.

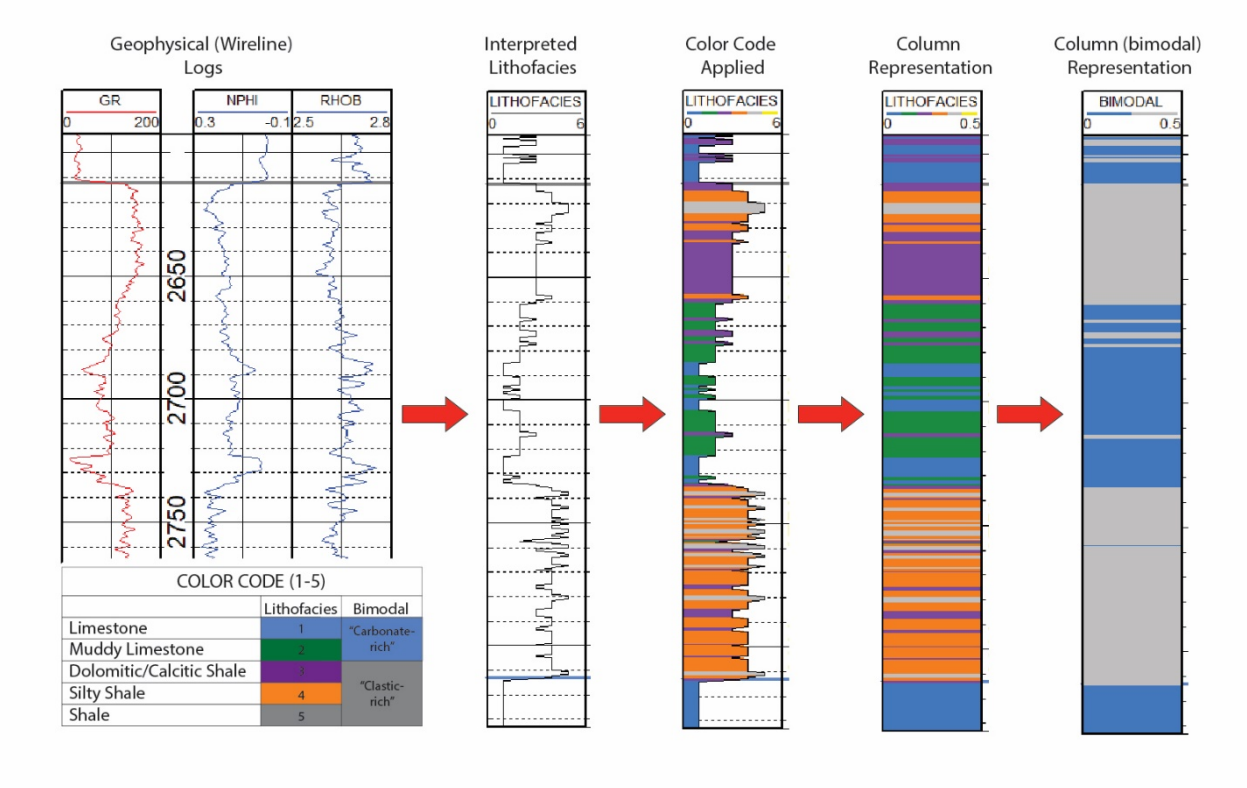

Figure 3.4. Schematic diagram showing the development of the lithofacies model from wireline logs.

3.1.1. Model Test

The lithofacies interpretation is based on two test wells. The different criteria allowed us to create a cross plot chart that serves as the base for interpreting other wells in the basin (Figure 3.3).

To test the model, we compared, in a single well, the pXRF data with the log-based interpretation and placed them side by side to evaluate the agreements or potential pitfalls between elemental abundance and lithofacies. When the well did not contain these two sets of data, we chose pairs of nearby wells having available elemental pXRF data and interpreted lithofacies. For example, a well in Owen County, Indiana (well ID# 125617) has pXRF data and is located near a well having a suite of logs located in Greene County, Indiana (well ID# 118307) (Figure 3.5).

In this case, the log-based lithology shows an upper zone of muddy limestone with thin clean limestone streaks. The thin limestone intervals are apparent on the Owen County plot, but the Ca values suggest a rock richer in clay/quartz than the logs indicate (Figure 3.5).

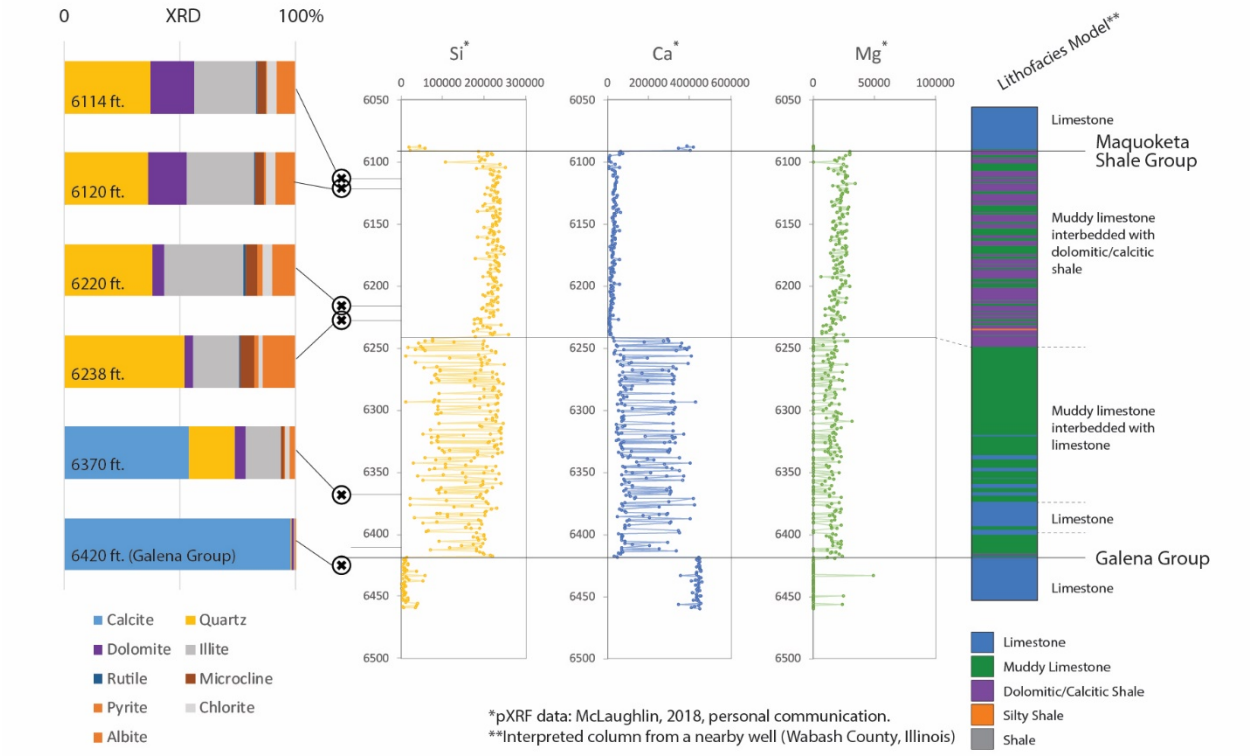

Figure 3.5. XRD and pXRF profiles in White County, Illinois. XRD results (left) show major mineralogy identified in six samples, one of which is part of the Trenton Limestone. Owing to the lack of wireline logs in the White County well, the interpretative column with the lithofacies representation on the right was taken from a nearby well in Wabash County, Illinois. Measured depths indicated on left of tracks are in feet.

3.1.2. Model Application and Regional Correlation

Cross sections made for the CarbonSAFE area illustrate the lateral variability of the Maquoketa Group (Appendix A). We interpret this variability in the context of the Maquoketa's potential to prevent upward, density-driven migration of hypothetically injected CO_2 into the underlain units (i.e., the unit and its subdivision's bulk permeability distribution).

A complete discussion and results of cross sections are included in section 4.

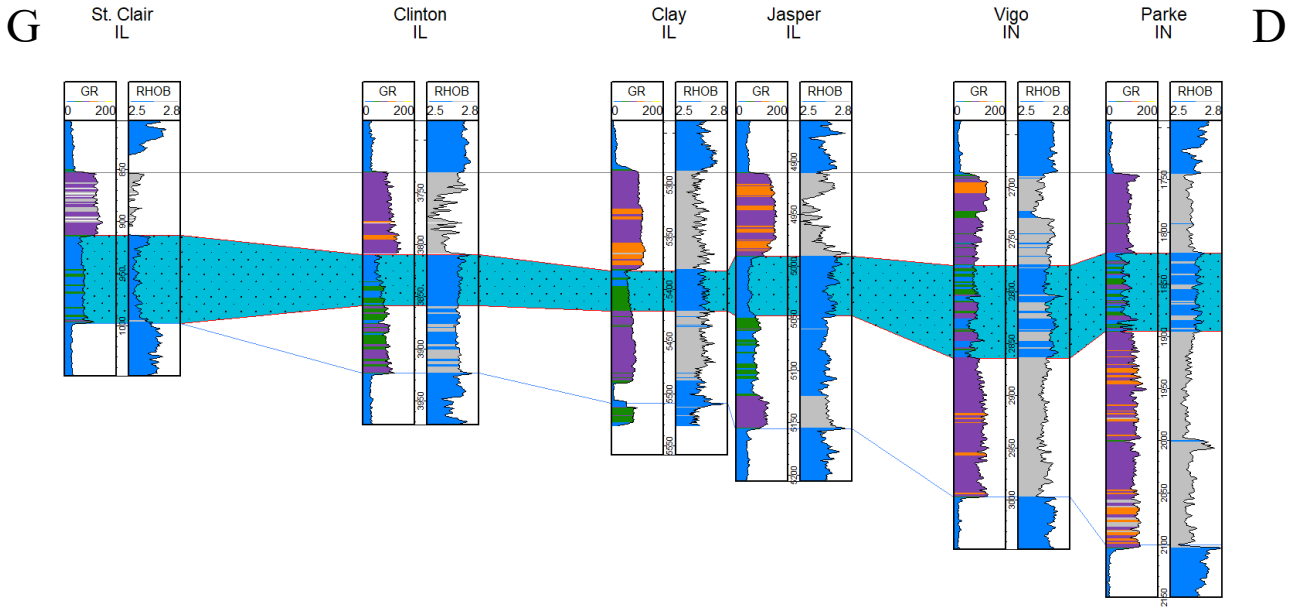

Figure 3.6: Cross section G-D (left to right) illustrating the thickness increase of the lower unit. A carbonate-rich unit identified in the middle section of the Maquoketa interval is highlighted. Depths in depth tracks are in feet. See Figure 3.4 for color codes. The location of the cross section is indicated in Figure A.1 (Appendix A).

3.1.3. Isopach Maps

The results of this model are portrayed as a series of net thickness maps for each lithofacies that reveal a high degree of regional variability in the Maquoketa Group lithofacies distribution (Figures 3.7–3.8).

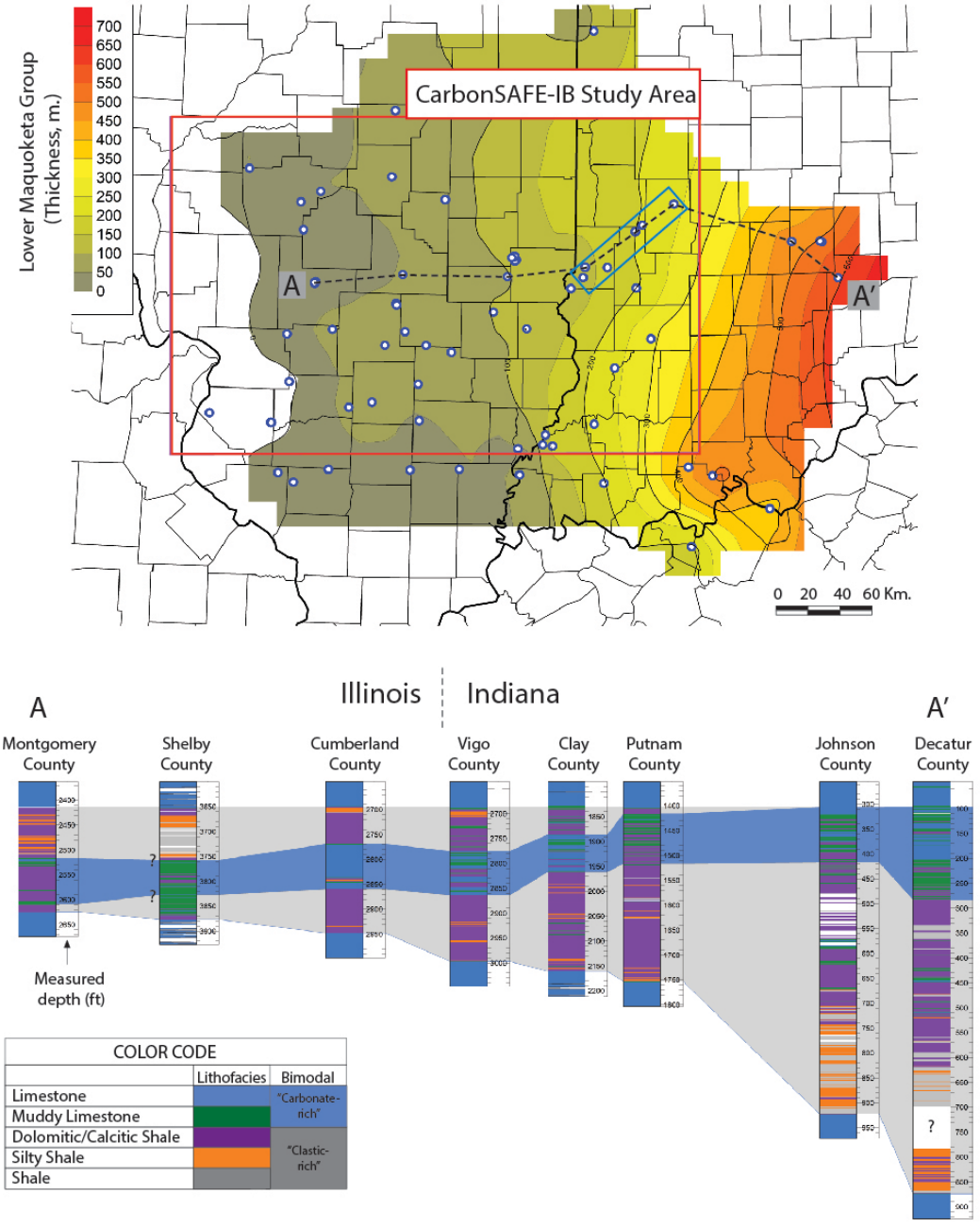

Figure 3.7. Isopach map and cross section of the lower Maquoketa Group in the CarbonSAFE-Illinois Basin (IB). The cross section illustrates the relative position of the middle unit that enhances the thickening of the lower unit. The blue rectangle on the map indicates the location of three wells from Vigo, Clay, and Putnam Counties in Indiana, which correlate with a lithostratigraphic subdivision published by Gray (1972) (Figure 4.1). Depths in depth tracks are in feet.

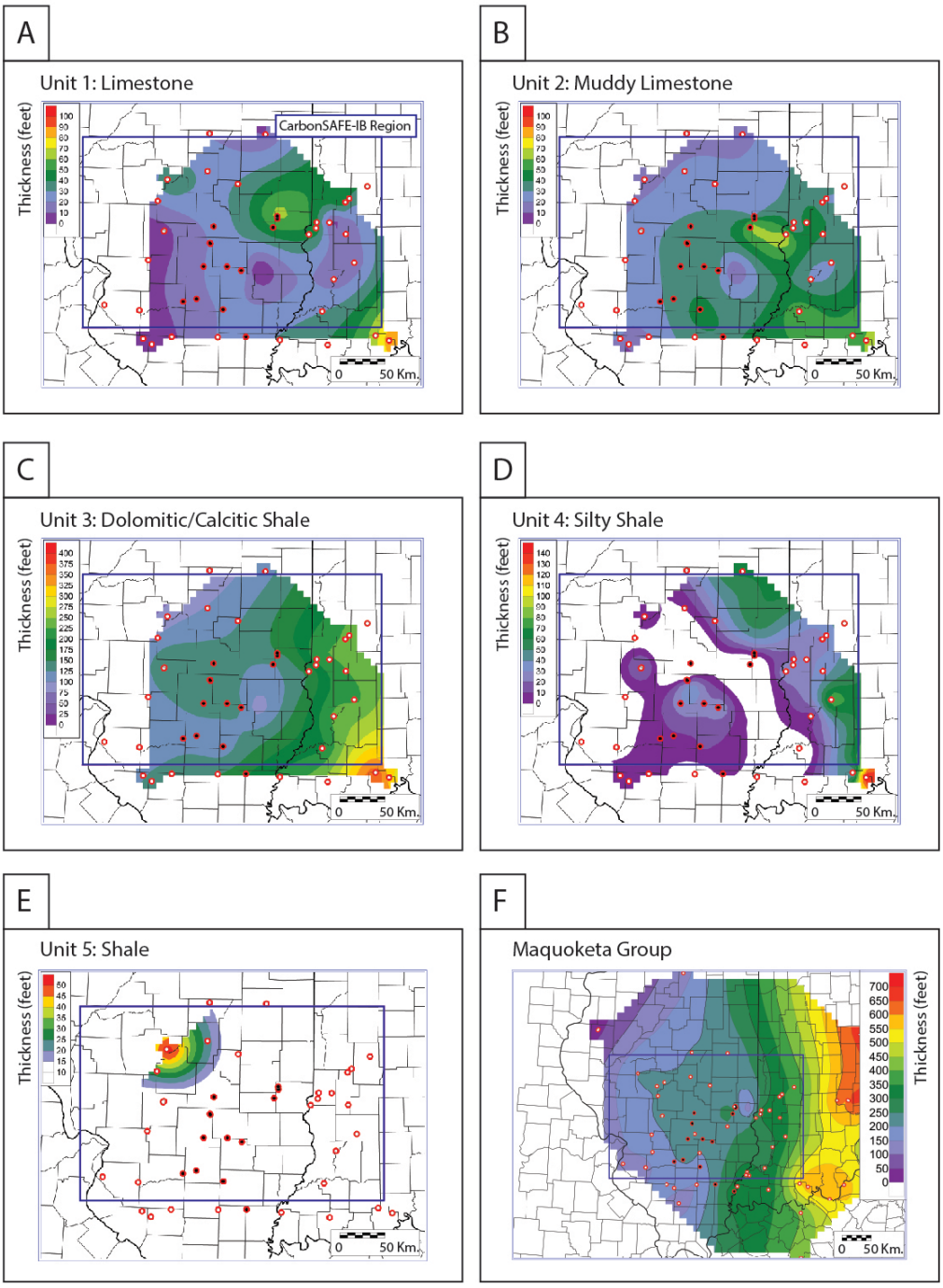

Figure 3.8 Isopach maps for all five lithofacies (A)–(E) and for the Maquoketa Group (F). The wells used for the interpolation are indicated in red.

3.2. MICP Analyses

3.2.1. Introduction

Mercury injection capillary pressure (MICP) is a widely used technique that provides quantitative information about pore structure, including total volume (porosity), pore surface area, pore size distribution, rock grain density, and permeability in porous solids. The Swanson model for determining permeability from capillary pressure curves was originally developed for sandstones and carbonates (Swanson, 1981). Later work incorporated mudstones and shales (Hildenbrand and Urai, 2003; Davudov et al., 2018). Mercury injection capillary pressure quantifies the pore-throat radius rather than the pore radius itself and, therefore, the pore-size distribution interpreted from this technique is referred to as 'pore-throat size distribution' (PSD). These properties are obtained by injecting a nonwetting phase, such as mercury, into a sample under increasing and controlled pressure steps. Larger pores will fill first at lower pressure steps, whereas smaller pores will fill as pressure increases.

The Maquoketa Group is a potential caprock seal unit for CO_2 sequestration sites in several states of the Midwest. Seal capacity is closely related to the minimum entry (threshold) pressure necessary to start saturating the pore system with fluids. The minimum pressure at which injected fluids start leaking or flowing through the seal is referred as to 'capillary entry pressure,' which can be determined using mercury porosimetry techniques (i.e., Tokunaga and Wan, 2013; Zhou et al., 2017).

Understanding capillary pressure and the drainage/imbibition curves from mercury porosimetry is important to quantify capillary trapping in reservoirs and seals. During injection, the supercritical CO_2 displaces the existing brine, and pores experience brine drainage. However, at the tail of the plume, the reservoir brine will partially reenter the pore system by imbibition processes (Joodaki et al., 2017).

3.2.2. Technique overview

Mercury injection capillary pressure has been used extensively in the petroleum industry to understand the properties of the top seal with respect to oil and gas migration (Daniel and Kaldi, 2009; Labani et al., 2013). The use of high-pressure MICP analysis offers an advantage over other methods because it provides indirect data about the distribution of pore size from nearly 1 nanometer up to nearly 1 mm (Figure 3.9).

One parameter used to calculate the pore-throat radius (r) is the contact angle between mercury and the solid surface. Although this value changes from mineral to mineral, Farokhpoor et al. (2013) suggested that it can be held constant because it does not change significantly during simulated CO_2 injection. The relationship between capillary pressure (Pc, in MPa) and pore-throat radius is quantified using the Washburn equation (Washburn, 1921):

$$P_c = -\frac{2*\gamma*\cos\theta}{r} \quad [3.1]$$

We analyzed 28 samples from 3 wells (Figure 3.10) with available samples (Appendix B: Table B.2) from the Maquoketa Group using a Micromeritics Autopore V 9620 that injects mercury up to 414 MPa (60,000 psia), which allows the analysis of pores of 0.003–360 microns. Each sample consisted of ~8–15 grams of fragments of about 5–10 mm in diameter each.

As pressure increases, the mercury intruding the pore system is measured by recording the displacement observed in the stem of the penetrometer (Figure 3.11). The values of mercury injected were corrected to account for conformance effects associated with low pressure required to surround the sample's

roughness with mercury. However, we did not include corrections associated with pore and grain compressibility, which can reduce porosity (Lan et al., 2017; Davudov et al., 2018).

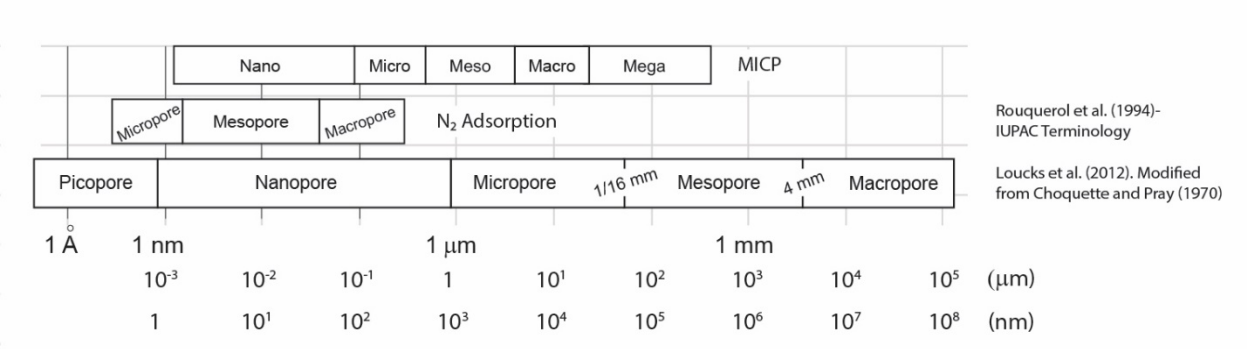

Figure 3.9. Pore size coverage and classification according to the technique used. The three horizontal bars correspond to MICP, gas adsorption, and thin section petrography, respectively.

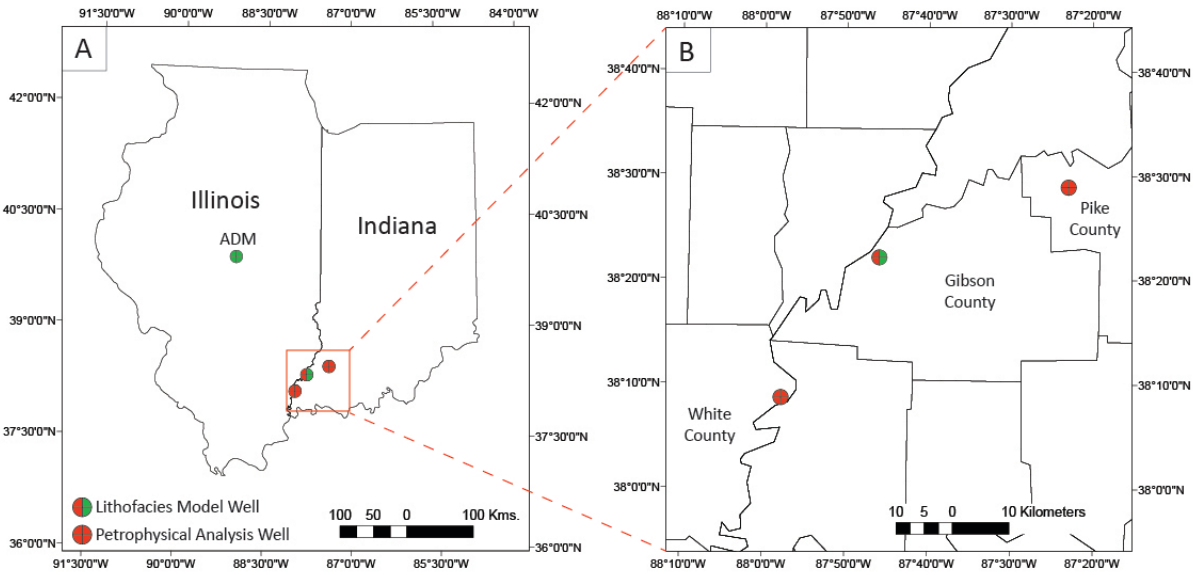

Figure 3.10: Study area indicating location of three wells studied.

3.2.3. Porosity from MICP

Porosity (ϕ) from MICP is calculated as follows:

$$\emptyset = \frac{V_{Hg}}{V_s} \qquad [3.2]$$

where V_{Hg} is the total volume of mercury that intruded the sample, which is reported after the MICP analysis has been performed, and Vs is the total volume of the sample, which is estimated as follows:

$$V_s = V_p - \left(\frac{W_a - W_p - W_s}{\rho_{Hg}}\right) \qquad [3.3]$$

where V_p is the volume of the penetrometer (calibrated, in mL); W_a is the weight of the apparatus loaded with sample and mercury (in g); W_p is the weight of the empty penetrometer (in g); W_s is the weight of the sample (in g); and ρ_{Hg} is the density of mercury (g/cm^3).

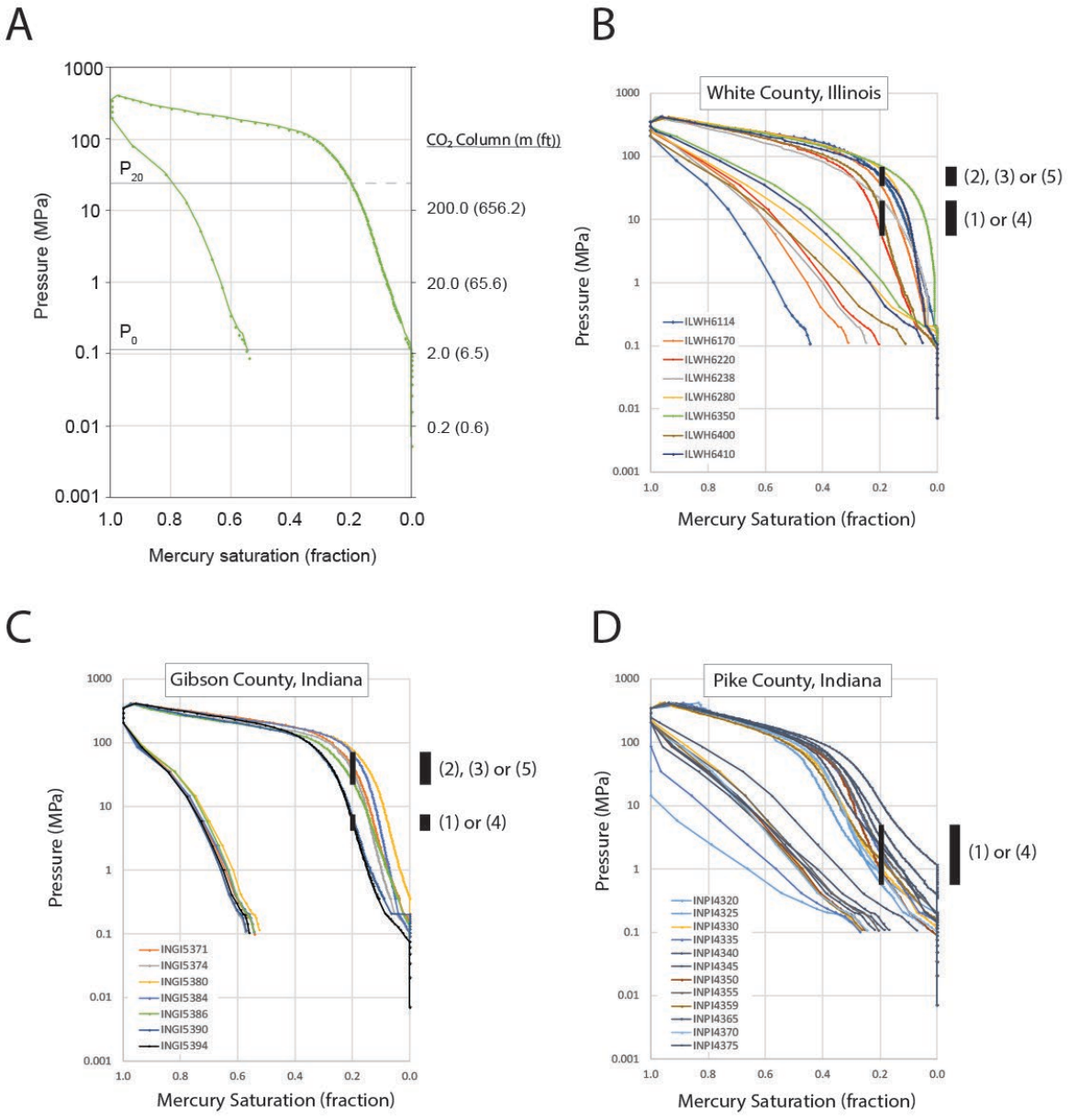

Figure 3.11. Capillary pressure curves indicating capillary entry pressure (P_0) and at 20 % saturation (P_{20}). The values indicated on the right are calculated using the conversion from mercury-air to CO_2-brine systems (see section 3.2.4). The bar on the right indicates the range of P_{20} and the possible lithofacies interpreted from these P_{20} values.

3.2.4. Permeability

In this work, we determined the permeability of samples using the Katz-Thompson method (Katz and Thompson, 1986). Permeability values derived from mercury porosimetry data are estimated using the following relationship:

$$k = C * d^2 * f \quad (3.4)$$

where k is permeability (in mD), C is a constant (4.3442), d is the characteristic length (μm) of the pore space associated with the pressure at which mercury first forms a continuous and connected pathway, and is determined experimentally from the incremental amount of mercury being injected at early stages of the mercury injection experiments. The value of f, termed 'conductivity formation factor' is also determined experimentally and reflects the connectedness of the pore space (Katz and Thompson, 1986). The values of permeability analyzed by the Autopore V9620 in this study employed this methodology (Appendix B: Table B.3). The observed permeability range was from 0.04 to 6.31. Minimum permeability was associated with lithofacies 3 (dolomitic/calcitic shale), and maximum permeability was associated with lithofacies 4 (silty shale).

In addition to MICP-based permeability (and porosity), a subset of samples (20) from Pike and Gibson Counties were sent to Weatherford Laboratories for crushed-core analyses (Figure 3.12). The results from these analyses are available in Appendix D (Table D.1; Figure D.2).

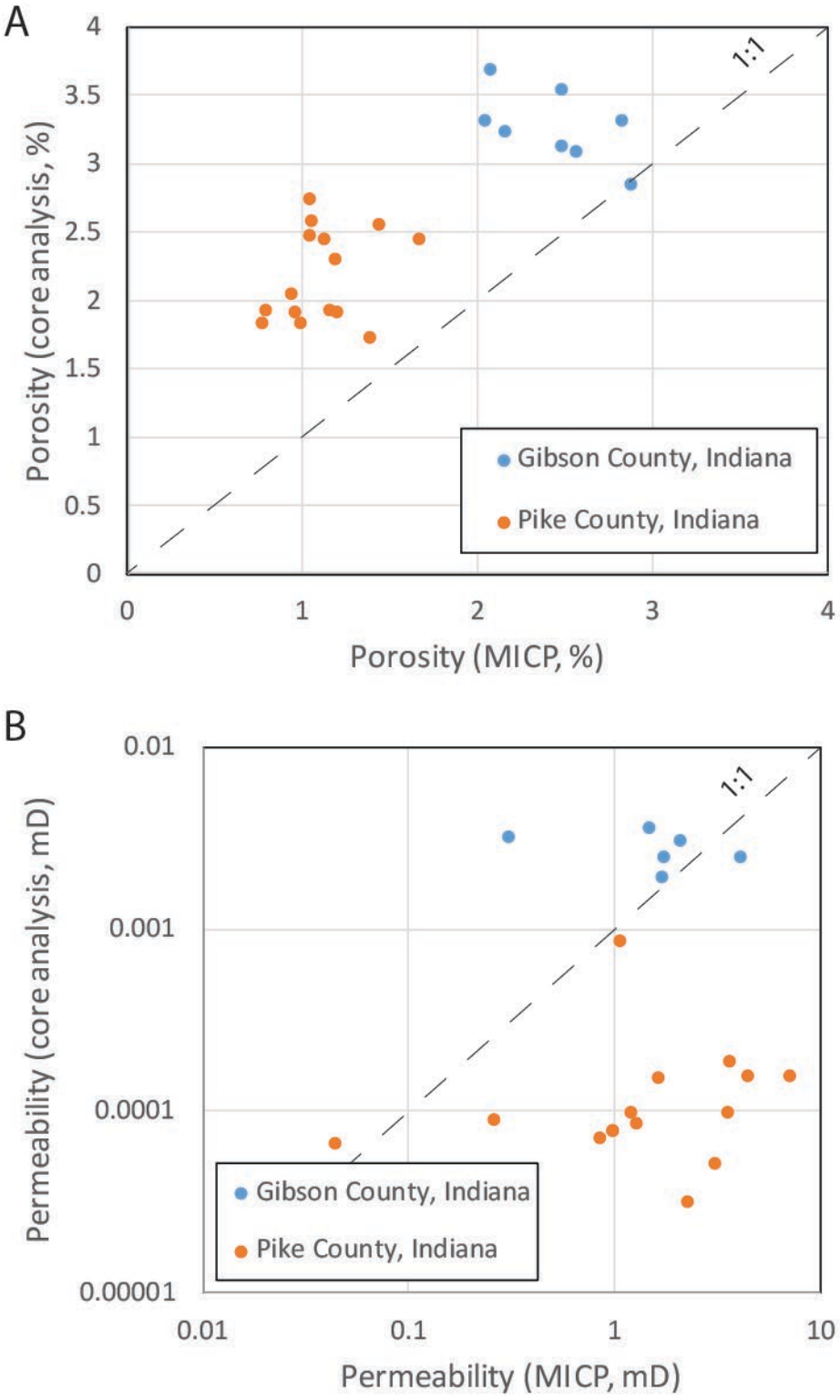

Figure 3.12. Scatter plots comparing porosity (A) and permeability (B) of the two techniques: MICP porosimetry (x-axis) and crushed-core analysis (y-axis).

3.2.5. Implications for Sealing Efficiency

Converting the values of capillary pressure at 0 % and 20 % of mercury intrusion (P_0 and P_{20}, respectively) into values of CO_2-gas column takes into consideration the surface tension and contact angle of the gas-brine and mercury-air system to first convert the measured mercury pressure values to CO_2-brine capillary pressure values (Vavra et al., 1992):

$$P_{C_{CO2-Brine}} = \frac{\gamma_{co2-brine}}{\gamma_{Hg-air}} x \left[\frac{cos\theta_{co2-brine}}{cos\theta_{Hg-air}}\right] x P_{C_{Hg-air}} \qquad (3.5)$$

where $P_{C_{CO2-Brine}}$ is the capillary pressure for the CO_2-water system; $\gamma_{co2-brine}$ is the interfacial tension of CO_2 and brine (60 mN/m); $\theta_{co2-brine}$ is the contact angle of CO_2 and brine (60°; Bachu and Bennion, 2009); γ_{Hg-air} is the interfacial tension of mercury and air (485 mN/m); θ_{Hg-air} is the contact angle of mercury and air against the solid (130°); and $P_{C_{Hg-air}}$ is the capillary pressure for the mercury-air system (experimentally determined). Applying these values in (3.5) we obtain:

$$P_{C_{CO2-Brine}} = 0.08\ x\ P_{C_{Hg-air}} \qquad (3.6)$$

Assuming a hydrostatic pressure gradient of 0.011 MPa/m (0.49 psi/ft) and a supercritical CO_2 density of 712 kg/m^3, brine density of 1150 kg/m^3, the associated pressure and CO_2 column for no intrusion (P_0), and for 20 % of saturation (P_{20}) into the caprock is calculated using the density-driven relationship for pressure (P_x reported in MPa and hence the 10^{-6} conversion factor) exerted on the seal/reservoir interface as follows (Table B.4):

$$Px = (\rho_{brine} - \rho_{CO2}) * g * h = 438 * 9.8 * 10^{-6} * \text{h} = 4292.4 * 10^{-6} * \text{h} \qquad (3.7)$$

or

$$h = 232.97 * Px \qquad (3.9)$$

Replacing (3.9) in (3.6) to convert from mercury-air system (lab) into CO_2-brine (reservoir) system:

$$h_0(m) = 18.63 * P_0 \quad (3.10)$$

and

$$h_{20}(m) = 18.63 * P_{20} \qquad (3.11)$$

These sets of equation allowed us to quantify an equivalent CO_2 column associated with capillary pressure obtained in the lab using a mercury porosimeter. Resultant values for CO_2 columns for all samples studied are discussed in the following chapter.

4. Conclusions and Discussions

The conclusions from the petrophysical characterization and lithofacies model developed in this work for the Maquoketa Group in the CarbonSAFE area include the following:

- The Maquoketa Group exhibits a heterogeneous character at different scales, including microscale (as suggested by SEM, pXRF, thin sections, and mercury porosimetry), and large-scale (meter) as suggested by wireline logs. The lithofacies model suggests that the Maquoketa Group can be subdivided into three main units: upper, middle, and lower, which is consistent with previously proposed stratigraphic subdivisions (Brainard Shale, Fort Atkinson Limestone, and Scales Shale, respectively) (Figure 4.1) (Gray, 1972). Overall, the relative stratigraphic position of the middle unit (carbonate-rich), varies from middle to lower (relative to the entire Maquoketa Group) in the west (shallower portions of the Illinois Basin), to upper in the deeper portions of the Illinois Basin towards the east. This trend can be observed in the cross sections (Figure 3.7; Appendix A).

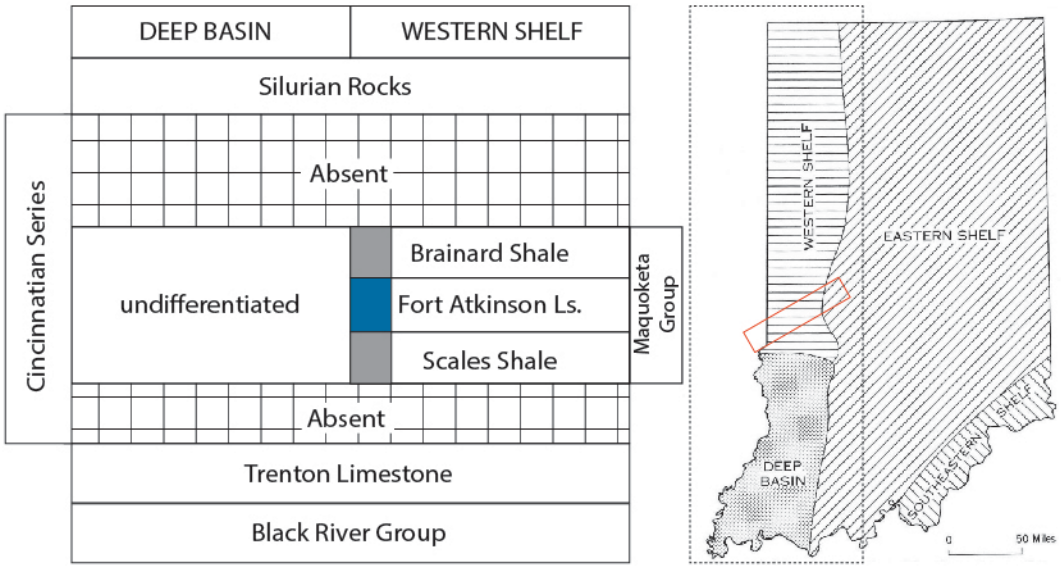

Figure 4.1. Lithostratigraphic nomenclature of the Maquoketa Group in western Indiana (modified from Gray, 1972). The names on western shelf follow definitions from the Illinois State Geological Survey (Kolata and Graese, 1983).

- The five lithologies quantified by the lithofacies model could serve to improve our knowledge of the lithological distribution within a complex unit such as the Maquoketa Group. However, the source of data used in the model include gamma-ray, neutron, and density logs, which in some cases are not accurate and must be corrected. The limited number of wells used in the study area followed a quality assurance/quality control (QA/QC) procedure. Several observations can be drawn from the lithofacies model portrayed in these cross sections, which are hung 50 ft above the top of the Maquoketa Group. These observations include the following:

    - A generalized subdivision of the Maquoketa Group can be established based on the predominance of an upper, middle, and lower unit. The upper unit is dominated by dolomitic/calcitic shale and silty shale. The middle unit is dominated by limestone and muddy limestone (in some regions this unit has been identified as the Fort Atkinson Limestone), and the lower unit is composed mostly of dolomitic/calcitic shale and, in minor amounts, muddy limestone and silty shale. This subdivision is consistent with previously published work (i.e., Gray, 1972; Kolata and Graese, 1983).

    - The lithofacies model included 50 ft above and below the top and bottom of the Maquoketa Group to assure that the interpretation includes the lower portion of the Silurian carbonates and the upper portion of the Trenton Limestone. This interpretation is consistent with the known stratigraphy, and cross sections show that these intervals are interpreted as limestone. An illustrative example explains the process of using the combination of wireline logs and how these data were portrayed as a five-lithofacies and two-color bimodal representation of the interpreted column (in blue in Figure 3.4).

    - The thickness of the lower unit of the Maquoketa Group increases to the east and was mapped; cross sections AE (Appendix A) and GD (Figure 3.6) show this trend. An isopach map and a cross section illustrates this trend (Figure 3.7).

    - The relative position of the carbonate-rich middle unit varies from the bottom of the Maquoketa Group in the southwest and the south to the top of the Maquoketa Group in the northeast (cross sections GD and FE, respectively). This work does not include geochronological data; this observation does not use a depositional framework, but rather should be seen as a compartmentalized unit for facilitating the interpretations of the sealing potential of the Maquoketa Group.

- The MICP and core analysis data document significantly different properties for the White, Gibson and Pike County samples. The core and MICP porosity data for Gibson and Pike Counties indicate that the Gibson County samples contain about 1.5 % greater porosity by core analysis than by MICP (2.5 % versus 1.0 %). The core analysis indicates about 1.0 % greater porosity for the Gibson County wells (3.25 % versus 2.25 %). Despite the greater porosity in the Gibson County well, the MICP-based permeability values for the two samples are very similar. The MICP analysis indicates similar values of permeability for both data sets (Figure 3.12). The presence of significantly greater porosity for the Gibson samples without significant increase in permeability suggests that a larger portion of the porosity of the Gibson samples is located in very small pores and contributes little to the bulk permeability. By implication, the average pore size for the Pike County samples is greater than for the Gibson samples. The suggestion of greater pore size for the Pike County samples is supported by the MICP Hg saturation/pressure plots. The Gibson and Pike County samples have similar entry pressures, indicating a similar volume of 'large' pores. This similarity in large pore size results in a similar interpretation of the CO_2 column heights for both samples when calculated for entry pressures (Figure 4.3, green data).

- The pressure associated with 20 % of mercury saturation (P_{20}) is about ten times larger for the samples from the Gibson County well than those from the Pike County well samples (Figure 4.3), resulting in greater seal potential for the Gibson County, Indiana, well. The P_{20} CO_2 column height calculation is controlled by the abundance of larger pores; that is, the greater relative abundance of large pores results in a lower Hg pressure at 20 % saturation which, in turn, results in a calculation of smaller P_{20} CO_2 column heights for the Pike County samples than for the White and Gibson County samples. The large pores in the Pike County samples are most likely located in the silty shale lithofacies present in the Pike County samples (Figure 4.4) but absent in the Gibson and White County samples.

- As determined by the model proposed in this work, relationships between lithofacies could shed light on the sealing efficiency of each associated lithology. In this context, the XRD results from core samples for the White County well suggest that samples are dolomitic/calcitic shale. This result is consistent with the resultant lithofacies (Figure 3.5). XRD analyses from two samples in the Pike County well also suggest that these samples are dolomitic/calcitic shale (Figure 4.4), but the core sample and the high amounts of quartz (interpreted from XRD in the core sample) might suggest that the sequence is composed of a series of interbedded dolomitic/calcitic shale and silty shale (Figure 4.4). The silty shale component could be related to the relative low seal potential as compared to other wells (Figure 4.3). A proposed relationship between capillary pressure (MICP) curves and lithofacies is shown in Figure 3.12.

- The results of porosity and permeability from core analyses (Weatherford Laboratories, pers. comm.) (Appendix D) show higher values of porosity than those obtained from MICP analyses. These values fall in the same order of magnitude (Figure 3.12A). However, the resulting values of permeability from crushed core analyses exhibit up to four order of magnitudes lower than the resulting values of permeability from MICP. Although no explanation is available at this point, we propose that this difference relies on the fact that the permeability obtained at Weatherford used an aggregation of grains that average 1 mm in diameter.

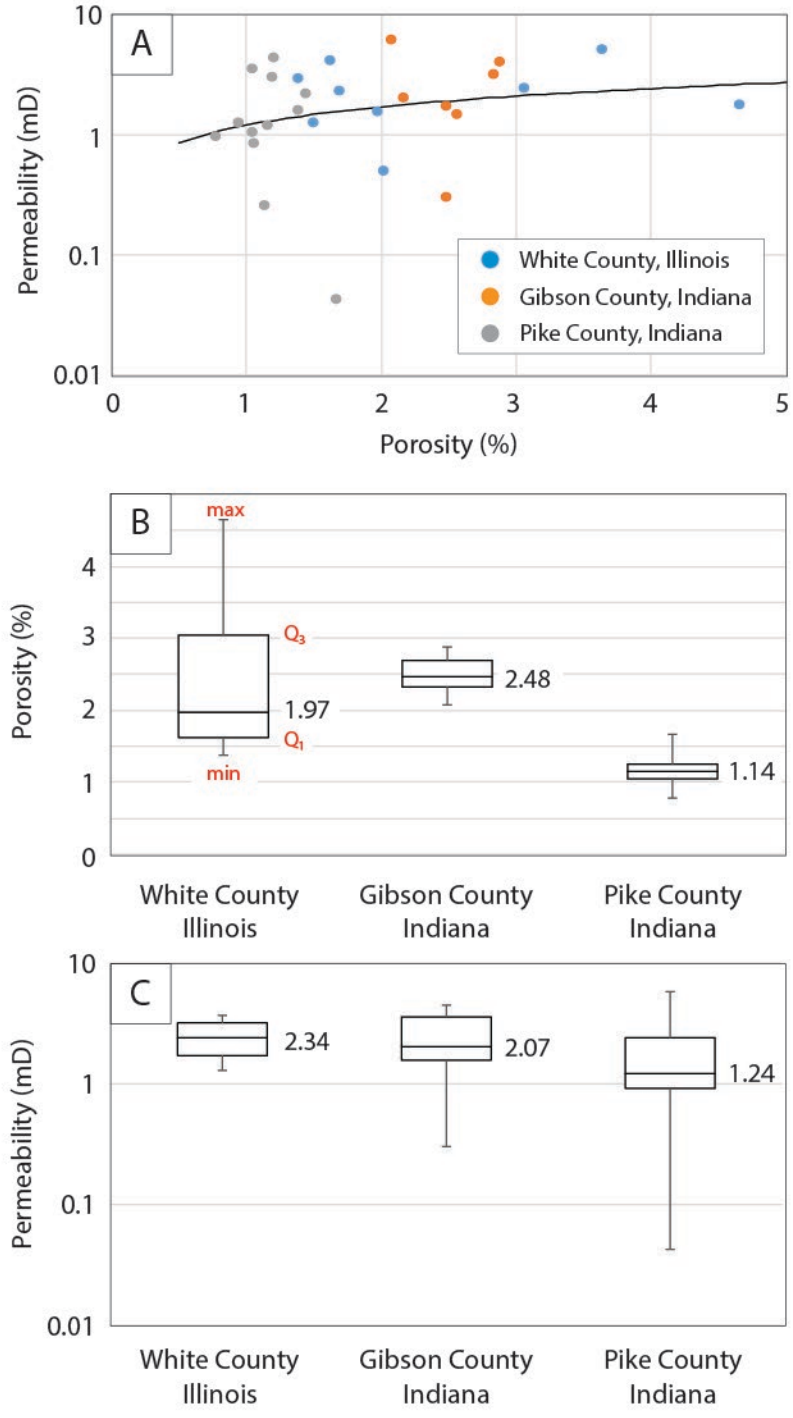

Figure 4.2. (A) Porosity-permeability relationship in samples from three wells. Box and whisker plots, also called box plots, indicate the five-number summary of a set of data for porosity (B) and permeability (C). The five-number statistics include minimum value, 25th quartile, 75th quartile, and maximum value (in red) and the median. The median values are posted in all charts (Source of image: Medina et al., Personal Comm.).

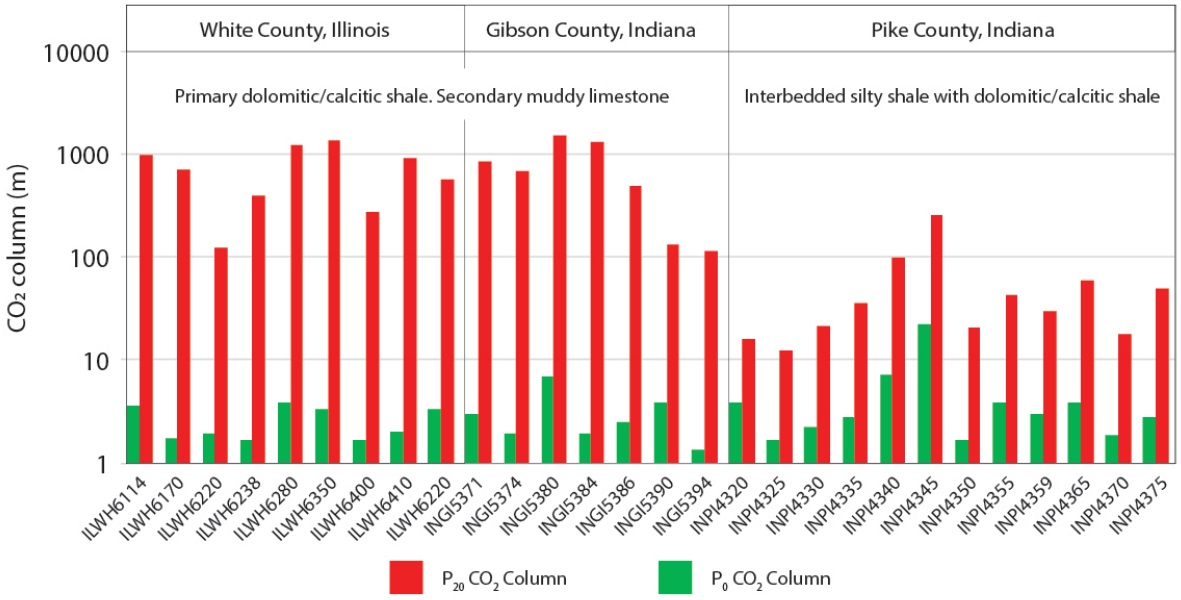

Figure 4.3. Calculated CO_2 (supercritical) column (in meters) using two values of capillary pressures (P_0 in green and P_{20} in red) (Source of image: Medina et al., Personal Comm.).

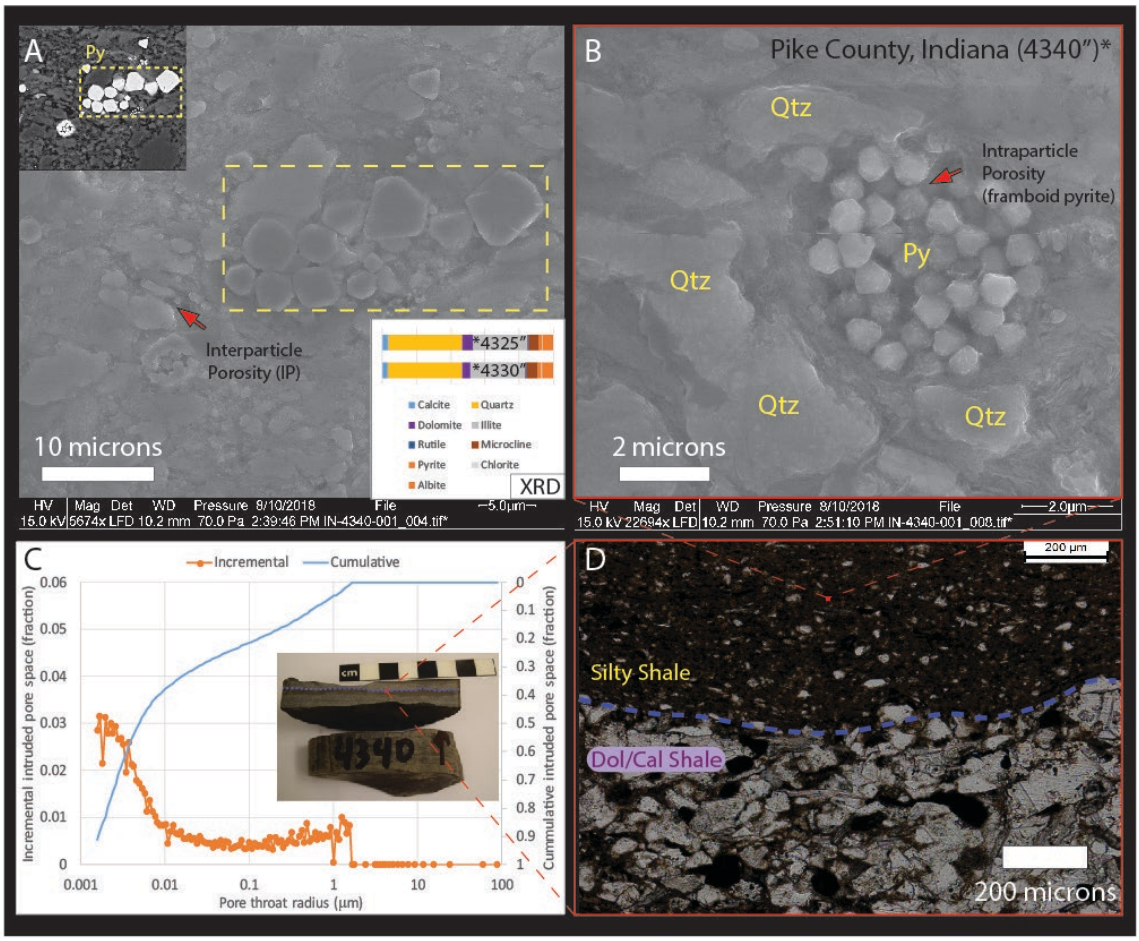

Figure 4.4. SEM images (A, B) indicating the presence of porosity hosted in framboid pyrite (Py) in sample INPI4340 (Pike County). The small picture in upper-left corner of (A) displays backscattered image highlighting pyrite; (C) shows the pore size distribution. Pores on the order of 0.1–1 micron in size are resolved with SEM images in (A) and (B), but are not detected from microphotographic techniques (D). *XRD results in the lower right corner of (A) confirms the presence of quartz, illite, and pyrite from nearby samples (INPI4325 and INPI4330) (Source of image: Medina et al., Personal Comm.).

5. References

Asquith, G. B., and Gibson, C. R., 1982, Basic well log analysis for geologists, Tulsa, Okla., USA, American Association of Petroleum Geologists, Methods in exploration series, 216 p.

Bachu, S. and D. B. Bennion, 2009, Interfacial tension between CO2, freshwater, and brine in the range of pressure from (2 to 27) MPa, temperature from (20 to 125) °C, and water salinity from (0 to 334 000) mg·L−1: Journal of Chemical & Engineering Data, v. 54 (3), p. 765-775.

Bentham, M., and G. Kirby, 2005, CO_2 Storage in Saline Aquifers: Oil & Gas Science and Technology—Rev. IFP, v. 60, No. 3, p. 559-567.

Choquette, P. W. and L. C. Pray, 1970, Geologic nomenclature and classification of porosity in sedimentary carbonates: AAPG Bulletin, v. 54, no. 2, p. 207-244.

Daniel, R. F. and J. G. Kaldi, 2009, Evaluating seal capacity of caprocks and intraformational barriers for CO2 containment, in M. Grobe, J. C. Pashin, and R. L. Dodge, eds., Carbon dioxide sequestration in geological media—State of the science: AAPG Studies in Geology 59, p. 335–345.

Davudov, D., Moghanloo, R. G., and Lan, Y., 2018, Evaluation of accessible porosity using mercury injection capillary pressure data in shale samples: Energy & Fuels, v. 32, no. 4, p. 4682-4694.

Ellett, K., Zhang, Q., Medina, C., Rupp, J., Wang, G., and T. Carr, 2013, Uncertainty in Regional-scale Evaluation of CO_2 Geologic Storage Resources—comparison of the Illinois Basin (USA) and the Ordos Basin (China): Energy Procedia, v. 37, no. 0, p. 5151-5159.

Farokhpoor, R., Bjørkvik, B. J. A., Lindeberg, E., and O. Torsæter, 2013, Wettability behaviour of CO2 at storage conditions: International Journal of Greenhouse Gas Control, v. 12, no. Supplement C, p. 18-25.

Gray, H. H., 1972, Lithostratigraphy of the Maquoketa Group (Ordovician) in Indiana. Department of Natural Resources Geological Survey Special Report 7. 31 pp.

Greb, S., Bowersox, J. R., Solis, M. P., Harris, D. C., Riley, R. A., Rupp, J. A., Kelley, M., and N. Gupta, 2012, Ordovician Knox carbonates and sandstones of the eastern midcontinent: Potential geologic carbon storage reservoirs and seals, in Derby, J. R., Fritz, R. D., Longacre, S. A., Morgan, W. A., and C. A. Sternbach, eds., The great American carbonate bank: The geology and economic resources of the Cambrian – Ordovician Sauk megasequence of Laurentia, AAPG Memoir 98, p. 1077-1101.

Hildenbrand, A., and Urai, J. L., 2003, Investigation of the morphology of pore space in mudstones—first results: Marine and Petroleum Geology, v. 20, no. 10, p. 1185-1200.

Joodaki, S., Yang, Z., and A. Niemi, 2017, The effect of designing parameter of WAG injection on enhancement of CO−2 trapping in heterogeneous formations: A numerical study: Greenhouse Gases: Science and Technology, v. 7, no. 6, p. 1008-1019.

Katz, A. J., and Thompson, A. H., 1986, Quantitative prediction of permeability in porous rock: Physical Review B, v. 34, no. 11, p. 8179.

Kolata, D. R., and Graese, A. M., 1983, Lithostratigraphy and depositional environments of the Maquoketa Group (Ordovician) in northern Illinois, Illinois State Geological Survey, Circular 528, 49 p.

Kolata, D. R., and Nelson, W.J., 1991. Tectonic history of the Illinois Basin. In: Leighton, M.W., Kolata, D.R., Oltz, D.F., Eidel, J.J. (eds.), Interior Cratonic Basins. AAPG Memoir 51, p. 263-285.

Labani, M. M., Rezaee, R., Saeedi, A., and A. A. Hinai, 2013, Evaluation of pore size spectrum of gas shale reservoirs using low pressure nitrogen adsorption, gas expansion and mercury porosimetry: A case study from the Perth and Canning Basins, Western Australia: Journal of Petroleum Science and Engineering, v. 112, p. 7-16.

Lan, Y., Moghanloo, R. G., and Davudov, D., 2017, Pore compressibility of shale formations.

Loucks, R. G., Reed, R. M., Ruppel, S. C., and U. Hammes, 2012, Spectrum of pore types and networks in mudrocks and a descriptive classification for matrix-related mudrock pores: AAPG Bulletin, v. 96, no. 6, p. 1071-1098.

Medina, C. R., Rupp, J. A., and D. A. Barnes, 2011, Effects of reduction in porosity and permeability with depth on storage capacity and injectivity in deep saline aquifers: A case study from the Mount Simon Sandstone aquifer: International Journal of Greenhouse Gas Control, v. 5, p. 146-156.

Medina, C. R., and J. A. Rupp, 2012, Reservoir characterization and lithostratigraphic division of the Mount Simon Sandstone (Cambrian): Implications for estimations of geologic sequestration storage capacity: Environmental Geosciences, v. 19, no. 1, p. 1-15.

Medina, C. R., Mastalerz, M., and J. A. Rupp, 2017, Characterization of porosity and pore-size distribution using multiple analytical tools: Implications for carbonate reservoir characterization in geologic storage of CO_2: Environmental Geosciences, v. 24, no. 1, p. 51-72.

Rouquerol, J., Avnir, D., Fairbridge, C. W., Everett, D. H., Haynes, J. M., Pernicone, N., Ramsay, J. D. F., Sing, K. S. W., and K. K. Unger, 1994, Recommendations for the characterization of porous solids (Technical Report): Pure Appl. Chem., v. 66, no. 8, p. 1739-1758.

Swanson, B. F., 1981, A simple correlation between permeabilities and mercury capillary pressures: Journal of Petroleum Technology, v. 33, p. 2498-2504.

Tokunaga, T. K., and J. Wan, 2013, Capillary Pressure and Mineral Wettability Influences on Reservoir CO2 Capacity: Reviews in Mineralogy and Geochemistry, v. 77, no. 1, p. 481-503.

Vavra, C. L., Kaldi, J. G., and R. M. Sneider, 1992, Geological applications of capillary pressure; a review: AAPG Bulletin, v. 76 (6), p. 840-850.

Washburn, E. W., 1921, Note on a method of determining the distribution of pore sizes in a porous material: Proceedings of the National Academy of Sciences of the United States of America, v. 7, no. 4, p. 115-116.

Zhou, Y., Hatzignatiou, D. G., and J. O. Helland, 2017, On the estimation of CO2 capillary entry pressure: Implications on geological CO2 storage: International Journal of Greenhouse Gas Control, v. 63, no. Supplement C, p. 26-36.

APPENDIX A: CROSS SECTIONS

Figure A.1. Location of cross sections. The dotted-line rectangle indicates the CarbonSAFE area shown in Figure 2.1.

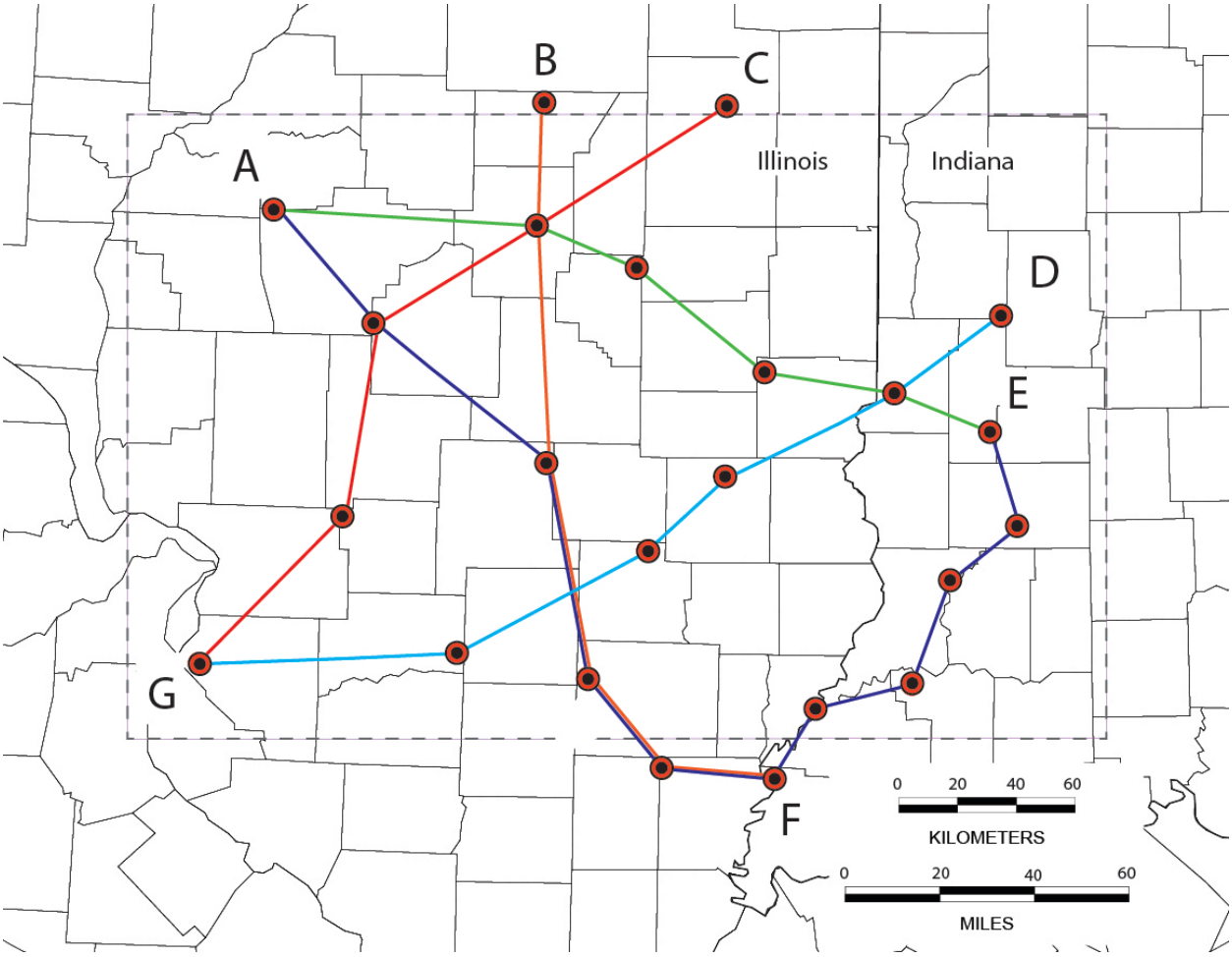

Figure A.2. Cross section A-E (left to right). A carbonate-rich unit identified in the middle section of the Maquoketa Group has been highlighted. Depth in depth tracks are in feet.

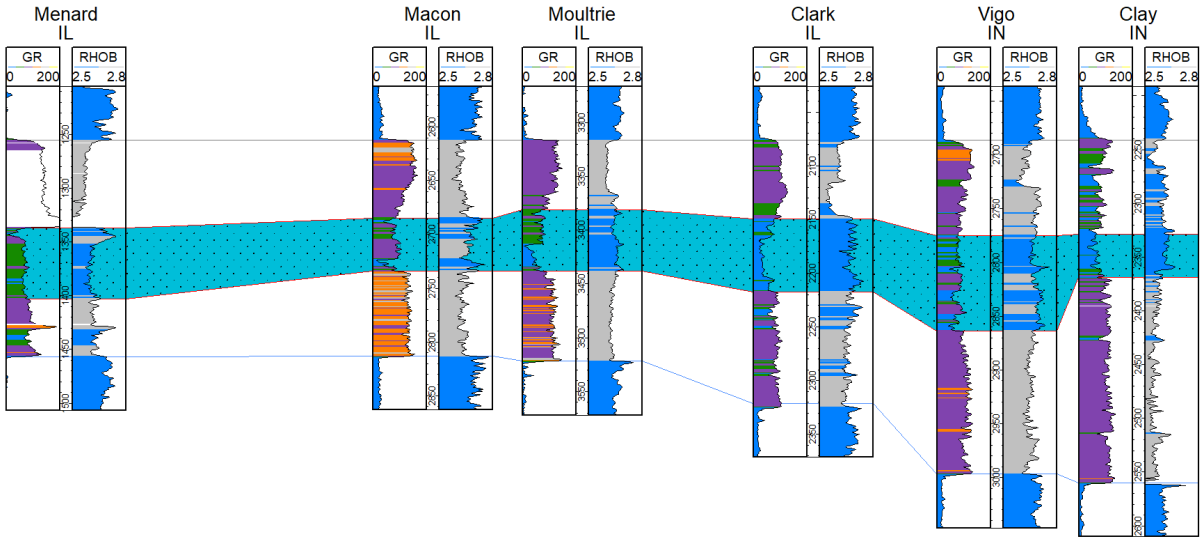

Figure A.3. Cross section A-F (left to right). A carbonate-rich unit identified in the middle section of the Maquoketa Group has been highlighted. Depth in depth tracks are in feet.

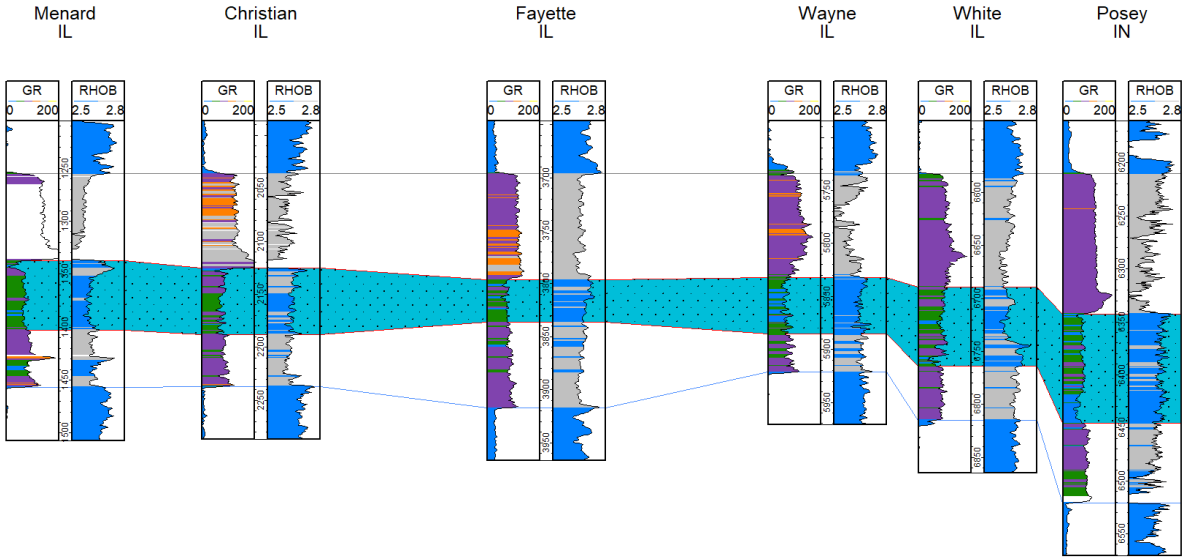

Figure A.4. Cross section B-F (left to right). A carbonate-rich unit identified in the middle section of the Maquoketa Group has been highlighted. Depth in depth tracks are in feet.

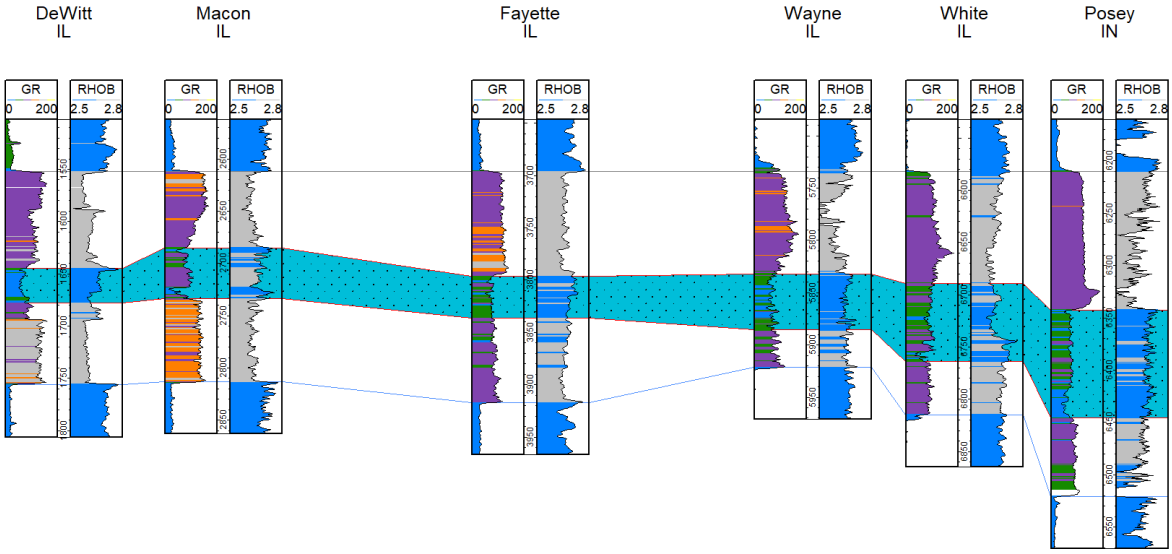

Figure A.5. Cross section G-C (left to right). A carbonate-rich unit identified in the middle section of the Maquoketa Group has been highlighted. Depth in depth tracks are in feet.

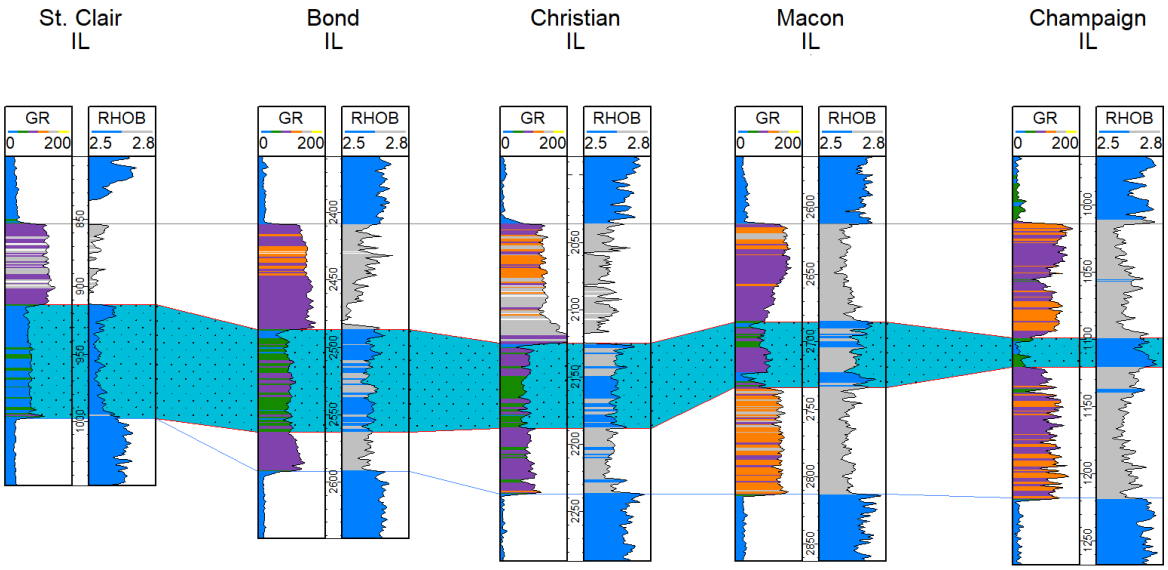

Figure A.6. Cross section F-E (left to right). A carbonate-rich unit identified in the middle section of the Maquoketa Group has been highlighted. Depth in depth tracks are in feet.

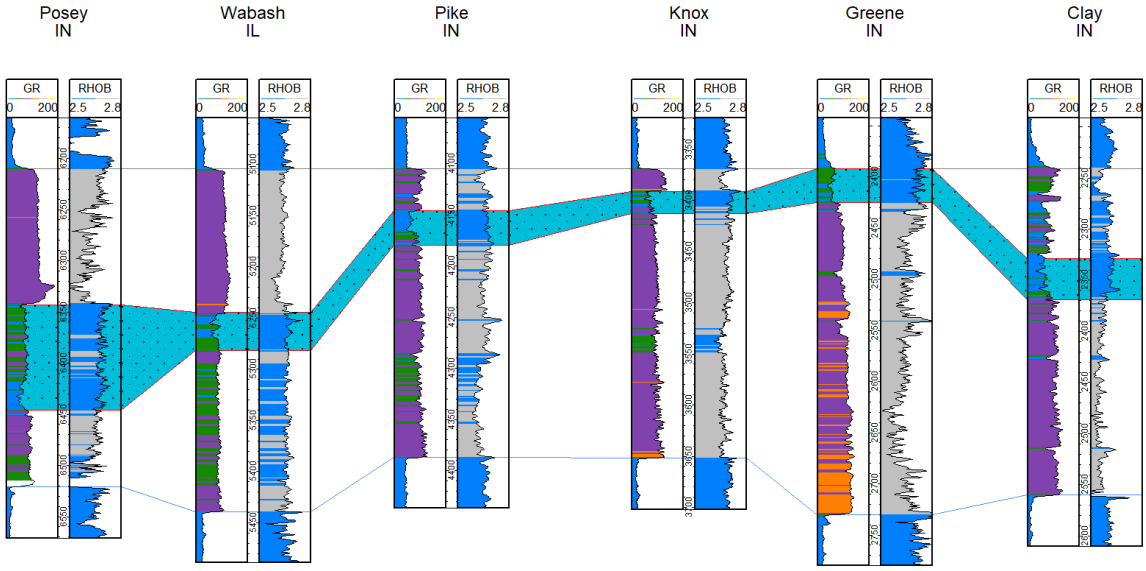

APPENDIX B: TABLES

Table B.1. Well ID, depth, and county location

Well ID	Sample ID	Depth		County	State
		ft	m		
121930469400	ILWH6114	6114.0	1863.5	White	Illinois
121930469400	ILWH6170	6170.0	1880.6	White	Illinois
121930469400	ILWH6220	6220.0	1895.9	White	Illinois
121930469400	ILWH6238	6238.0	1901.3	White	Illinois
121930469400	ILWH6280	6280.0	1914.1	White	Illinois
121930469400	ILWH6350	6350.0	1935.5	White	Illinois
121930469400	ILWH6400	6400.0	1950.7	White	Illinois
121930469400	ILWH6410	6410.0	1953.8	White	Illinois
121930469400	ILWH6458	6458.0	1968.4	White	Illinois
166184	INGI5371	5371.5	1637.2	Gibson	Indiana
166184	INGI5374	5374.0	1638.0	Gibson	Indiana
166184	INGI5380	5380.0	1639.8	Gibson	Indiana
166184	INGI5384	5384.0	1641.0	Gibson	Indiana
166184	INGI5386	5386.5	1641.8	Gibson	Indiana
166184	INGI5390	5390.0	1642.9	Gibson	Indiana
166184	INGI5394	5394.0	1644.1	Gibson	Indiana
164185	INPI4320	4320.0	1316.7	Pike	Indiana
164185	INPI4325	4325.0	1318.3	Pike	Indiana
164185	INPI4330	4330.0	1319.8	Pike	Indiana
164185	INPI4335	4335.0	1321.3	Pike	Indiana
164185	INPI4340	4340.0	1322.8	Pike	Indiana
164185	INPI4345	4345.0	1324.4	Pike	Indiana
164185	INPI4350	4350.0	1325.9	Pike	Indiana
164185	INPI4355	4355.0	1327.4	Pike	Indiana
164185	INPI4359	4359.0	1328.6	Pike	Indiana
164185	INPI4365	4365.0	1330.5	Pike	Indiana
164185	INPI4370	4370.0	1332.0	Pike	Indiana
164185	INPI4375	4375.0	1333.5	Pike	Indiana

Table B.2. List of samples and analyses performed on each sample

Sample ID	Sample Depth (m)	pXRF	N_2 Adsorption	MICP
ILWH6110	1862.3		X	
ILWH6114	1863.5	X	X	X
ILWH6120	1865.4		X	
ILWH6170	1880.6	X	X	X
ILWH6220	1895.9	X	X	X
ILWH6238	1901.3		X	X
ILWH6280	1914.1	X	X	X
ILWH6290	1917.2	X		
ILWH6300	1920.2	X		
ILWH6302	1920.8	X	X	
ILWH6308	1922.7		X	
ILWH6350	1935.5	X	X	X
ILWH6370	1941.6		X	
ILWH6390	1947.7	X		
ILWH6400	1950.7			X
ILWH6410	1953.8			X
ILWH6420*	1956.8		X	
ILWH6430*	1959.9		X	
ILWH6440*	1962.9	X	X	
ILWH6458*	1968.4	X	X	X
INGIB5366	1635.7	X	X	
INGIB5371	1637.1	X	X	X
INGIB5374	1638.0	X	X	X
INGIB5380	1639.8	X	X	X
INGIB5384	1641.2	X	X	X
INGIB5386	1641.8	X	X	X
INGIB5390	1642.9	X	X	X
INGIB5394	1644.1	X	X	X
INPI4320	1316.7	X	X	X
INPI4325	1318.3	X	X	X
INPI4330	1319.8	X	X	X
INPI4335	1321.3	X	X	X
INPI4340	1322.8	X	X	X
INPI4345	1324.4	X	X	X
INPI4350	1325.9	X	X	X
INPI4355	1327.4	X	X	X
INPI4359	1328.6	X	X	X
INPI4365	1330.5	X	X	X
INPI4370	1332.0	X	X	X
INPI4375	1333.5	X	X	X

Table B.3. Mercury injection capillary pressure results

Mercury Porosimetry (MICP)												
Sample ID	Total pore area at 59,980.88 psia	Median pore diameter (from volume)	Median pore diameter (from area)	Average pore diameter (4V/A)	Bulk density at 1.03 psia	Apparent (skeletal) density at max pressure	Porosity	Permeability (Katz)	Threshold Pressure	Entry Pressure	Pressure at 20% Sat. (P_{20})	
	m^2/g	nm	nm	nm	g/mL	g/mL	%	mD	psi	MPa	psi	MPa
ILWH6114	3.36	9.88	4.70	8.97	2.677	2.732	2.02	--	26.98	0.18602	7500.0	51.7
ILWH6170	5.89	7.79	4.38	7.70	2.695	2.780	3.06	2.4970	12.82	0.08839	5300.0	36.5
ILWH6220	2.00	27.91	4.55	11.44	2.622	2.662	1.50	1.2846	24.96	0.17209	4237.6	29.2
ILWH6238	5.80	13.26	4.89	9.71	2.582	2.680	3.64	5.2489	12.35	0.08515	3000.0	20.7
ILWH6280	2.35	18.08	4.61	10.62	2.713	2.760	1.69	2.3416	28.98	0.19981	9317.8	64.2
ILWH6350	9.53	8.30	4.55	7.62	2.564	2.689	4.65	1.7785	25.31	0.17451	10500.0	72.4
ILWH6400	1.94	34.78	4.84	12.33	2.710	2.755	1.62	4.2269	12.51	0.08625	2070.0	14.3
ILWH6410	3.35	9.93	4.70	8.60	2.729	2.784	1.97	1.5685	14.90	0.10273	7000.0	48.3
ILWH6458	0.25	215.37	36.33	91.95	2.685	2.726	1.51	3.1595	12.81	0.08832	200.0	1.4
INGI5371	4.29	9.16	4.44	8.70	2.656	2.723	2.48	1.7424	22.22	0.15320	6500.0	44.8
INGI5374	4.72	9.07	4.97	9.18	2.658	2.737	2.88	4.0467	14.56	0.10039	5252.0	36.2
INGI5380	4.32	8.68	4.63	8.62	2.659	2.727	2.48	0.3062	52.31	0.36066	11552.5	79.7
INGI5384	4.04	7.59	4.68	8.03	2.660	2.719	2.16	2.0707	14.48	0.09984	10008.8	69.0
INGI5386	4.22	8.89	5.28	9.12	2.662	2.732	2.56	1.4751	18.59	0.12817	3672.5	25.3
INGI5390	4.04	14.71	4.95	10.45	2.681	2.759	2.83	3.2138	28.97	0.19974	1011.5	7.0
INGI5394	3.36	11.83	4.46	9.26	2.664	2.721	2.07	6.3120	10.17	0.07012	876.0	6.0
INPI4320	0.55	6580.26	5.06	21.08	2.653	2.674	0.77	0.9666	28.82	0.19871	120.0	0.8
INPI4325	1.08	1973.68	4.81	16.67	2.654	2.686	1.20	4.4044	12.71	0.08763	93.0	0.6
INPI4330	1.44	408.02	4.77	15.13	2.628	2.666	1.43	2.2504	16.79	0.11576	160.0	1.1
INPI4335	0.78	3295.66	4.92	18.08	2.679	2.704	0.94	1.2792	20.91	0.14417	270.0	1.9
INPI4340	0.97	1854.25	4.80	17.58	2.644	2.674	1.13	0.2578	54.96	0.37894	750.0	5.2
INPI4345	1.55	922.88	4.70	16.41	2.621	2.666	1.67	0.0436	168.40	1.16108	1926.8	13.3
INPI4350	1.06	399.12	4.93	14.73	2.659	2.687	1.04	3.5704	12.86	0.08867	155.9	1.1
INPI4355	0.89	2840.13	4.88	17.80	2.635	2.663	1.05	0.8504	28.86	0.19898	320.3	2.2
INPI4359	1.27	652.98	4.85	16.59	2.638	2.675	1.39	1.6175	22.84	0.15748	223.6	1.5
INPI4365	1.09	887.43	4.90	16.00	2.658	2.689	1.15	1.2018	28.86	0.19898	459.6	3.2
INPI4370	1.10	1295.12	4.81	16.41	2.638	2.670	1.19	3.0471	14.03	0.09673	135.1	0.9
INPI4375	1.08	306.45	4.71	14.59	2.651	2.679	1.04	1.0510	20.76	0.14314	369.3	2.5

Table B.4. Source of data used in pressure analysis displayed in Figure 4.3

Sample ID	Subsurface Pressure		CO_2 Density	Delta Density (ρbrine-ρ_{CO2})	Entry Pressure (P_0)	CO_2 Column (P_0)		Pressure at 20% Sat. (P_{20})	CO_2 Column (P_{20})	
	psi	MPa	kg/m^3	kg/m^3	MPa	m	ft	MPa	m	ft
ILWH6114	2995.86	20.66	722.02	427.98	0.19	3.6	11.7	51.7	994.3	3262.1
ILWH6170	3023.30	20.84	722.11	427.89	0.09	1.7	5.6	36.5	702.8	2305.7
ILWH6220	3047.80	21.01	722.18	427.82	0.17	3.3	10.9	29.2	562.0	1843.8
ILWH6238	3056.62	21.07	722.21	427.79	0.09	1.6	5.4	20.7	397.9	1305.4
ILWH6280	3077.20	21.22	722.27	427.73	0.20	3.8	12.6	64.2	1236.0	4055.1
ILWH6350	3111.50	21.45	722.38	427.62	0.17	3.4	11.0	72.4	1393.2	4570.7
ILWH6400	3136.00	21.62	722.45	427.55	0.09	1.7	5.4	14.3	274.7	901.2
ILWH6410	3140.90	21.66	722.47	427.53	0.10	2.0	6.5	48.3	929.0	3047.8
ILWH6458	3164.42	21.82	722.54	427.46	0.09	1.7	5.6	1.4	26.5	87.1
INGI5371	2632.04	18.15	720.91	429.09	0.15	2.9	9.6	44.8	859.5	2819.8
INGI5374	2633.26	18.16	720.92	429.08	0.10	1.9	6.3	36.2	694.5	2278.5
INGI5380	2636.20	18.18	720.93	429.07	0.36	6.9	22.7	79.7	1527.6	5011.9
INGI5384	2638.16	18.19	720.93	429.07	0.10	1.9	6.3	69.0	1323.5	4342.2
INGI5386	2639.39	18.20	720.94	429.06	0.13	2.5	8.1	25.3	485.6	1593.3
INGI5390	2641.10	18.21	720.94	429.06	0.20	3.8	12.6	7.0	133.8	438.8
INGI5394	2643.06	18.22	720.95	429.05	0.07	1.3	4.4	6.0	115.8	380.1
INPI4320	2116.80	14.59	719.34	430.66	0.20	3.8	12.5	0.8	15.8	51.9
INPI4325	2119.25	14.61	719.35	430.65	0.09	1.7	5.5	0.6	12.3	40.2
INPI4330	2121.70	14.63	719.36	430.64	0.12	2.2	7.3	1.1	21.1	69.2
INPI4335	2124.15	14.65	719.36	430.64	0.14	2.8	9.0	1.9	35.6	116.7
INPI4340	2126.60	14.66	719.37	430.63	0.38	7.2	23.8	5.2	98.8	324.2
INPI4345	2129.05	14.68	719.38	430.62	1.16	22.2	72.8	13.3	253.9	832.9
INPI4350	2131.50	14.70	719.39	430.61	0.09	1.7	5.6	1.1	20.5	67.4
INPI4355	2133.95	14.71	719.39	430.61	0.20	3.8	12.5	2.2	42.2	138.5
INPI4359	2135.91	14.73	719.40	430.60	0.16	3.0	9.9	1.5	29.5	96.6
INPI4365	2138.85	14.75	719.41	430.59	0.20	3.8	12.5	3.2	60.6	198.7
INPI4370	2141.30	14.76	719.42	430.58	0.10	1.8	6.1	0.9	17.8	58.4
INPI4375	2143.75	14.78	719.42	430.58	0.14	2.7	9.0	2.5	48.7	159.7

APPENDIX C: MEASURED DEPTH

Figure C.1. Measured depth (in feet) of the Maquoketa Shale Group. Areas where the top of the unit is shallower than 2,500 ft are grayed out.

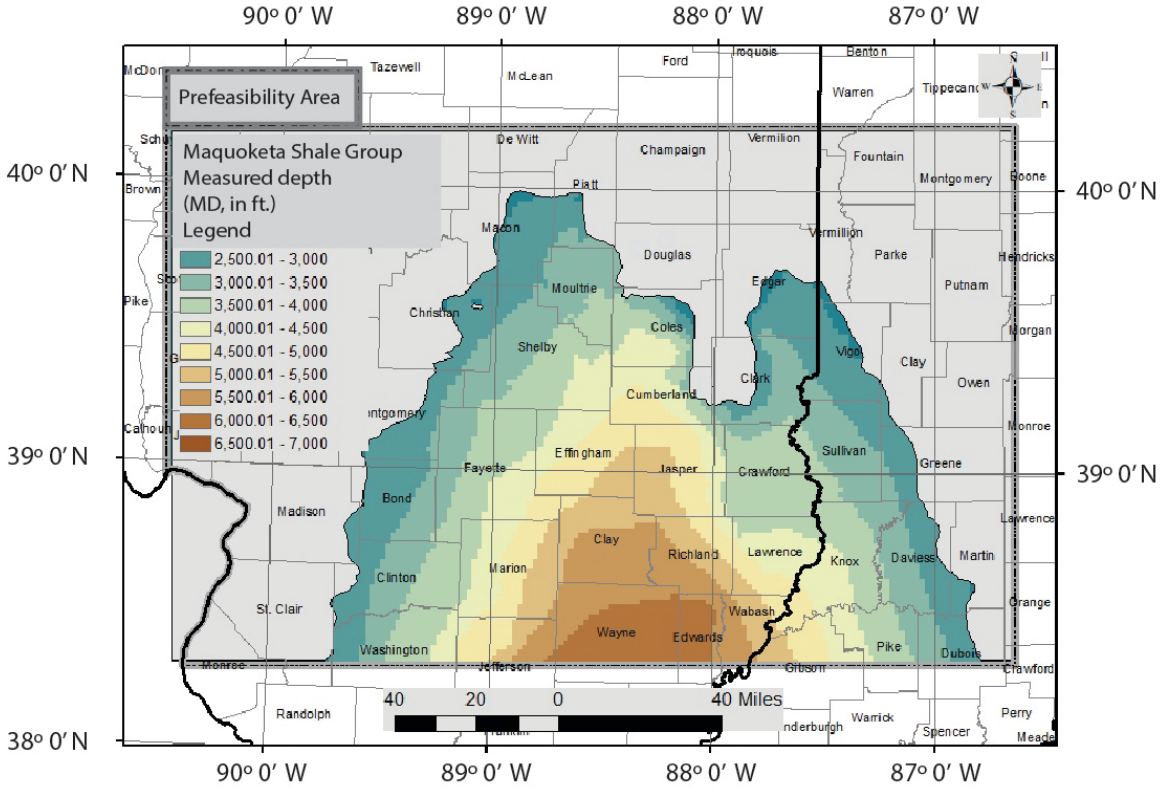

APPENDIX D. CRUSHED ROCK ANALYSIS BY WEATHERFORD LABORATORIES

D.1. Tabular Data

Weatherford LABORATORIES

Crushed Rock Analysis
Summary of Routine Crushed Core Analyses Results

As-Received and Vacuum Dried at 212°F

Indiana Geological Survey — HH-102035
CarbonSAFE Perm Project — 11/5/2018
Pike and Gibson County, IN

WFT Sample ID	Client Sample ID	Sample Depth, feet	A-R Bulk Density, gm/cc	Dry Bulk Density, gm/cc	Dry Grain Density, gm/cc	Dry Helium Porosity, % of BV	*Dry Press Decay Permeability, md*
1 CRA	INPI4320	4320.00	2.65	2.63	2.68	1.8	*7.83E-05*
2 CRA	INPI4325	4325.00	2.67	2.65	2.70	1.9	*1.55E-04*
3 CRA	INPI4330	4330.00	2.65	2.62	2.69	2.6	*3.17E-05*
4 CRA	INPI4335	4335.00	2.67	2.66	2.71	2.1	*8.59E-05*
5 CRA	INPI4340	4340.00	2.66	2.64	2.71	2.4	*8.96E-05*
6 CRA	INPI4345	4345.00	2.67	2.64	2.71	2.4	*6.71E-05*
7 CRA	INPI4350	4350.00	2.65	2.63	2.70	2.7	*1.86E-04*
8 CRA	INPI4355	4355.00	2.66	2.63	2.70	2.6	*7.21E-05*
9 CRA	INPI4359	4359.00	2.68	2.66	2.71	1.7	*1.52E-04*
10 CRA	INPI4365	4365.00	2.67	2.66	2.71	1.9	*9.75E-05*
11 CRA	INPI4370	4370.00	2.64	2.62	2.69	2.3	*5.16E-05*
12 CRA	INPI4375	4375.00	2.66	2.64	2.70	2.5	*8.57E-04*
13 CRA	INGIB5366	5366.50	2.68	2.66	2.76	3.5	*3.59E-03*
14 CRA	INGIB5371	5371.00	2.69	2.66	2.76	3.5	*2.52E-03*
15 CRA	INGIB5374	5374.00	2.72	2.70	2.78	2.9	*2.49E-03*
16 CRA	INGIB5380	5380.00	2.69	2.66	2.75	3.1	*3.19E-03*
17 CRA	INGIB5384	5384.50	2.69	2.67	2.76	3.2	*3.09E-03*
18 CRA	INGIB5386	5386.60	2.69	2.67	2.75	3.1	*3.63E-03*
19 CRA	INGIB5390	5390.10	2.72	2.70	2.79	3.3	*1.95E-03*
20 CRA	INGIB5394	5394.00	2.68	2.65	2.76	3.7	*1.05E-03*
Average values:			2.67	2.65	2.73	2.7	*1.17E-03*

As-received bulk volumes and bulk densities were determined on intact bulk sample material.
The bulk material was crushed and all other analysis reported herein were conducted on the crushed material.

Permeabilities calculated using PD mathematics.

D.2. Permeability versus percentage total porosity, dry crushed preparation